BIOCHEMISTRY
including biophysical chemistry & molecular biology
Article

Biochemistry **2010,** *49,* 7323–7343 7323
DOI: 10.1021/bi100588a

Congruency between Biophysical Data from Multiple Platforms and Molecular Dynamics Simulation of the Double-Super Helix Model of Nascent High-Density Lipoprotein†

Valentin Gogonea,*[,‡,§,⊥] Zhiping Wu,[§,⊥] Xavier Lee,[§,⊥] Vitaliy Pipich,[@] Xin-Min Li,[§,⊥] Alexander I. Ioffe,[@] Joseph A. DiDonato,[§,⊥] and Stanley L. Hazen*[,§,⊥,∥]

[‡]*Department of Chemistry, Cleveland State University, Cleveland, Ohio 44115,* [§]*Department of Cell Biology,* [∥]*Department of Cardiovascular Medicine, and* [⊥]*Center for Cardiovascular Diagnostics and Prevention, Cleveland Clinic, Cleveland, Ohio 44195, and* [@]*Jülich Center for Neutron Research at the FRM-II, Forschungscentrum, Jülich GmbH, D-85747 Garching, Germany*

Received April 16, 2010; Revised Manuscript Received July 2, 2010

ABSTRACT: The predicted structure and molecular trajectories from >80 ns molecular dynamics simulation of the solvated Double-Super Helix (DSH) model of nascent high-density lipoprotein (HDL) were determined and compared with experimental data on reconstituted nascent HDL obtained from multiple biophysical platforms, including small angle neutron scattering (SANS) with contrast variation, hydrogen−deuterium exchange tandem mass spectrometry (H/D-MS/MS), nuclear magnetic resonance spectroscopy (NMR), cross-linking tandem mass spectrometry (MS/MS), fluorescence resonance energy transfer (FRET), electron spin resonance spectroscopy (ESR), and electron microscopy. In general, biophysical constraints experimentally derived from the multiple platforms agree with the same quantities evaluated using the simulation trajectory. Notably, key structural features postulated for the recent DSH model of nascent HDL are retained during the simulation, including (1) the superhelical conformation of the antiparallel apolipoprotein A1 (apoA1) chains, (2) the lipid micellar−pseudolamellar organization, and (3) the solvent-exposed Solar Flare loops, proposed sites of interaction with LCAT (lecithin cholesteryl acyltransferase). Analysis of salt bridge persistence during simulation provides insights into structural features of apoA1 that forms the backbone of the lipoprotein. The combination of molecular dynamics simulation and experimental data from a broad range of biophysical platforms serves as a powerful approach to studying large macromolecular assemblies such as lipoproteins. This application to nascent HDL validates the DSH model proposed earlier and suggests new structural details of nascent HDL.

High-density lipoproteins (HDL)[1] are complex macromolecular assemblies that function to transport free and esterified cholesterol cargo from periphery cells to liver for ultimate elimination from the body through a complex physiological process called reverse cholesterol transport (*1*, *2*). HDL continue to be the focus of intense clinical, biological, and structural investigations because of substantial evidence indicating a crucial role for the lipoprotein in atherosclerosis (*3*−*5*). HDL historically are defined by their buoyant density characteristics and constitute a complex array of apolipoprotein A1 (apoA1)-containing particles that differ on the basis of their degree of maturation and composition, including the suite of proteins associated with the HDL particle. The heterogeneous nature of HDL and the plasticity and dynamics of the molten particle are essential features for the lipid carrying biological function. However, these same characteristics have impeded detailed structural interrogation of HDL and the ability to relate specific physiological functions of the particle to defined structural features. Theoretical models of nascent HDL, an early form of HDL formed upon lipidation of apolipoprotein A1 by the ABCA1 cell transporter, have evolved as new experimental data have accumulated and been applied to the refinement of existing models [e.g., Picket Fence (*6*), Double Belt (*7*, *8*), various Hairpin Loop types (*9*−*11*), Solar Flares (*12*), and, most recently, the Double-Super Helix Model (DSH)(*13*)].

Traditional high-resolution structural approaches such as X-ray crystallography and NMR have thus far proven to be ineffective for structural characterization of intact HDL. Consequently, many global structure−function relationships of the lipoprotein have been inferred by molecular dynamics simulations, and most of the all atom structures of nascent HDL proposed thus far are computational models with limited experimental data (*14*−*22*). A growing movement within the structural biology field for the study of macromolecular complexes resistant to traditional high-resolution approaches is the concept of combining synergistic data from multiple diverse experimental techniques through computationally intensive theoretical methodologies. In theory, it is thus possible to enhance lower-resolution

†This study was supported by National Institutes of Health Grants P01 HL098055, P01 HL076491-055328, P01 HL087018-02001, and R01 DK080732-01.

*To whom correspondence should be addressed: Cleveland State University, 2121 Euclid Ave., SI 422, Cleveland, OH 44115, or Cleveland Clinic, 9500 Euclid Ave., NE1-221, Cleveland, OH 44195. E-mail: v.gogonea@csuohio.edu or hazens@ccf.org. Telephone: (216) 445-9763. Fax: (216) 636-0392.

[1]Abbreviations: apoA1, apolipoprotein A1; DSH, Double Super Helix; EM, electron microscopy; ESR, electron spin resonance spectroscopy; FRET, fluorescence resonance energy transfer; H/D-MS/MS, hydrogen−deuterium exchange tandem mass spectrometry; HDL, high-density lipoprotein(s); LCAT, lecithin cholesteryl acyltransferase; MPO, myeloperoxidase; MS/MS, cross-linking tandem mass spectrometry; NMR, nuclear magnetic resonance spectroscopy; PH, patch hydrophobicity; pHDL, plasma-derived HDL; POPC, 1-palmitoyl-2-oleoyl-*sn*-glycero-3-phosphocholine; rHDL, reconstituted nascent high-density lipoprotein; rmsd, root-mean-square displacement; SANS, small angle neutron scattering; SASA, solvent accessible surface area; SUV, small unilamellar vesicles.

Published on Web 07/15/2010

models to greater refinement, bridging gaps in results and conclusions from individual platforms (*13*, *23*−*25*).

For example, a mechanistic understanding of membrane protein structure and function can be achieved without crystallographic or alternative high-resolution data by combining biophysical and biochemical constraints with computational analyses and cryo-EM low-resolution data (*26*). In this spirit, we have recently proposed a new structural model of nascent HDL, the Double-Super Helix (DSH) model, by combining for the first time small angle neutron scattering (SANS) with contrast variation and biophysical constraints from multiple platforms with computational modeling (*13*). Low-resolution structures of protein and lipid components of nascent HDL were directly visualized by SANS with contrast variation and selective isotopic deuteration of apoA1 and then enhanced by incorporation of additional biophysical constraints [e.g., hydrogen−deuterium exchange tandem mass spectrometry (H/D-MS/MS), fluorescence resonance energy transfer (FRET), MS/MS cross-links, electron microscopy (EM), and electron spin resonance spectroscopy (ESR)].

Key structural features of the DSH model, namely, the open helical shape of apoA1 and a nonbilayer organization of the lipid phase around the protein scaffold (*13*), are a dramatic departure from the widely held view of nascent HDL as a lipid bilayer disk enshrined by a circular belt of protein. While the DSH model proposed was derived from computational approaches that incorporated biophysical constraints from multiple diverse platforms, a detailed analysis of the model following prolonged molecular dynamics simulation has not yet been reported. In these studies, we more closely examine the relationship between available experimental data for reconstituted nascent HDL obtained by various biophysical approaches and an all-atom 80 ns molecular dynamics simulation analysis of the fully hydrated particle. The phospholipid:cholesterol:protein ratio of the reconstituted HDL particles examined in this study is comparable to that reported for ABCA1-generated nascent HDL (e.g., ref *27*), and structure−function studies of the reconstituted HDL particles by our group has previously shown they possess biological activities indistinguishable from HDL isolated from plasma, including promotion of cholesterol efflux activity, LCAT interaction and activation, anti-inflammatory and anti-apoptotic activity, and specific binding to the HDL receptor, scavenger receptor B1 (*12*, *13*). Our main goal in this study was to investigate whether molecular dynamics simulations are congruent with SANS imaging data; i.e., we tried to answer the following question: Is the helical shape of the protein component of nascent HDL thermodynamically feasible?

MATERIALS AND METHODS

Preparation and Routine Characterization of Nascent HDL. All reconstituted nascent HDL (rHDL) preparations generated for SANS, NMR, and EM analyses in these studies were first characterized by an array of biophysical (e.g., dynamic light scattering, nondenaturing PAGE, and far-UV circular dichroism), chemical (e.g., confirmation of chemical composition by LC−MS/MS analysis of select amino acids for protein quantification, cholesterol, phospholipid, and cholate), and biochemical assays [i.e., total and ABCA1-dependent cholesterol efflux, interaction with the plasma enzyme lethicin cholesteryl acyltransferase (LCAT), binding to the HDL receptor (scavenger receptor B1, SRB1), and both anti-apoptotic and anti-inflammatory activities] to ensure generation of a relatively monodisperse, chemically and biologically defined, and functionally intact particle. A detailed presentation of the methods used to prepare rHDL and the biophysical, chemical, biochemical, and functional assays used for its characterization have recently been extensively described (*13*). In brief, human apoA1 was isolated from HDL recovered from the plasma of healthy donors by ultracentrifugation, and lipid free human apoA1 was isolated by ion exchange chromatography of delipidated HDL (*28*). Recombinant human apoA1 was generated in *Escherichia coli* (*29*) using the kanamycin resistant plasmid pET20b+ encoding six-His-tagged human apoA1 transformed into *E. coli* BL21(DE3) cells (*13*). Deuterated recombinant human apoA1 was similarly prepared from *E. coli* grown in >90% D_2O and deuterated nutrients (*13*). Sodium cholate dialysis (*30*) was used to prepare rHDL using 1-palmitoyl-2-oleoyl-*sn*-glycero-3-phosphocholine (POPC), cholesterol, and apoA1 in a molar ratio of 100:10:1. Before being used in SANS, EM, or NMR studies, rHDL and isolated human plasma-derived HDL (pHDL) preparations were further purified by gel filtration chromatography using a large (approximately 1 in. × 3 ft) Sephacryl S300 (GE Healthcare) column.

Small Angle Neutron Scattering Analyses. SANS experiments were conducted on instrument KW2 (http://www.jcns.info/detailsKWS2), a classical pinhole camera that provides the highest neutron flux available at the Jülich Center for Neutron Science at reactor FRM-II (Garching, Germany). Data were collected from two positions of the detector (2 and 8 m from the sample), thus covering the momentum transfer (q) range from 0.008 to 0.35 $Å^{-1}$. The wavelength λ of the neutron beam used was 4.5 Å. As in recently reported studies (*13*), samples were measured at multiple levels of contrast, including those optimized to visualize the protein within rHDL (i.e., in 12% D_2O, the match point of lipid) and those optimized to visualize the lipid within rHDL (i.e., in 42% D_2O, the match point of protein). Analyses of the scattering intensities at each contrast level produced the radius of gyration, R_g [using Guinier approximation (*31*)], and the intensity extrapolated to 0°. First, GNOM (*32*) was used to deconvolute the scattering intensity curve into the distance distribution function, $p(r)$, using the inverse Fourier transformation. The $p(r)$ function was subsequently used for DAMMIN (*32*) to produce low-resolution structures of both the protein and the lipid components of nascent HDL based on data from 12 and 42% D_2O contrast levels, respectively. The signal:noise ratio of the sample in 12% D_2O was enhanced using deuterated apoA1 for the reconstitution of the HDL particle.

^{31}P NMR Experiments with Nascent HDL and Small Unilamellar Vesicles. rHDL, pHDL, and small unilamellar vesicles (SUV) were comprised of 1-palmitoyl-2-oleoyl-*sn*-glycero-3-phosphocholine (POPC) generated by extrusion. POPC was selected for the generation of small unilamellar vesicles (SUV) because X-ray diffraction studies have demonstrated this molecular species of glycerophospholipid preferentially adopts the lamellar phase (*33*, *34*). To prepare SUV, POPC in chloroform was initially dried under vacuum and then fully hydrated by addition of buffer [20 mM Hepes buffer and 100 mM NaCl in 10% D_2O (pH 7.4)] above the phase transition temperature (*35*). Following vortexing to disperse the hydrated lipids, SUV were generated by sequential extrusion through polycarbonate filters with 0.4, 0.1, 0.05, and 0.03 mm pore sizes multiple times using an Avanti Mini-Extruder Set (Avanti Polar Lipids, Alabaster, AL). Throughout all experiments, freshly prepared vesicles were maintained well above the phase transition temperature to avoid vesicle fusion. The hydrodynamic radius of SUV preparations

was determined with a DynaPro-801 dynamic light scattering instrument as described previously (*12*), and ^{31}P NMR analyses of HDL and SUV preparations were performed on a Varian Inova 600 MHz spectrometer operating at 242.85 MHz equipped with a broadband probe. Spectra were recorded with WALTZ-16 modulated proton decoupling (599.91 MHz) at 30 °C. The chemical shift positions of lipid dispersions and HDL were recorded relative to 85% H_3PO_4 (0.00 ppm).

Electron Microscopy Studies. Images of negatively stained HDL were recorded as recently described (*13*) using a JEOL 1200 EX II microscope at 100 kV, and selected negatives were digitized on a Zeiss scanner at a step size of 14 μm giving a pixel size of 3.5 Å at the specimen level. The resulting data were processed further with the Imagic package.

Solvation of the DSH Model of Nascent HDL. The Double Super Helix (DSH) model used as the starting structure of the simulation is deposited in the Protein Data Bank (PDB) as entry 2K2S. To shorten the simulation time, the all-atom model of nascent HDL (the DSH model) was converted to an united-atom model using well-established force fields within the GROMACS molecular dynamics simulation program (*36*) to describe the interactions between atoms of molecules composing the lipoprotein and solvent. In this type of force field [modified GROMOS87 force field in GROMACS (*36*)], hydrophobic hydrogen atoms, and the carbon atom to which they attach (CH_3, CH_2, and CH), are replaced by united atoms that have a volume that accommodates all atoms in the group. To describe the interaction among atoms of phospholipids (POPC), a modified united-atom force field with special parameters for acyl chains was used (*37*, *38*). Cholesterol was described by a united-atom force field developed by Höltje and Brandt (*39*). Next, the united-atom model of nascent HDL (here termed the DSH model) was solvated in water using a previously described protocol (*12*). Briefly, the DSH model was immersed in a box of SPC water molecules (*40*). The distance from the particle to solvent box walls was set to 1.5 nm to minimize the interaction of the lipoprotein with its images in the replicas. Eight water molecules were replaced with sodium ions to neutralize the negative charge of the two chains of apoA1, and then 48 water molecules were substituted with 24 pairs of NaCl ions to produce a physiological salt concentration in the simulation box (300 mosM). The solvated system was subjected to a series of energy minimizations, using GROMACS, in which the system was allowed to relax gradually (first the solvent alone, then the lipid, and finally the protein). In the last step of energy minimization, all atoms in the system were allowed to relax. The calculation of the total energy of the system has taken into account periodic boundary conditions for the solvated system; the cutoff for the van der Waals interactions was 1 nm, and for Coulomb interactions, the Ewald summation was used as implemented in the PME method (*41*).

Molecular Dynamics Simulation on Solvated Nascent HDL. Prior to the 80 ns simulation of HDL, a preliminary 100 ps simulation of the particle was performed where movement of all non-hydrogen atoms of the lipoprotein were restrained to allow the solvent to rearrange and start equilibrating. In addition, the change in temperature, the total energy, and the root-mean-square displacement (rmsd) of the protein backbone were monitored during the entire simulation. By 20 ns, all of these variables achieve a steady state level. The simulation was performed in a canonical ensemble, *NVT* (i.e., the variable of states number of particles, *N*, volume, *V*, and absolute temperature, *T*, were kept constant). The simulation *T* was maintained at 300 K using the Berendsen thermostat (*42*). Random initial velocities were assigned for 300 K. The bonds between atoms in protein and lipid components were reset to their correct value by using the LINCS algorithm (*43*). Both the bond lengths and the bond angles in the water molecules were constrained by the SETTLE algorithm (*44*). The time integration step was 2 fs, and a coordinate frame was saved each 10 ps. All snapshots (more than 8000) constitute the trajectory of the particle during simulation, which was used to evaluate the quality of the simulation and the thermodynamic stability of the lipoprotein−solvent system. A trajectory made of 21 snapshots taken every nanosecond between 0 and 10 ns, and every 5 ns between 15 and 60 ns, was used for time-consuming analyses. While the initial 20 ns of simulation can be seen as system equilibration, this period was included in the analysis to compile a comprehensive understanding of where the model started, versus its steady state position following prolonged molecular dynamics simulation. This allowed us to more readily compare the impact of the simulation trajectory on the global architecture of apoA1, as well as the experimentally derived DSH model versus the penultimate model derived following the prolonged molecular dynamics simulation.

Calculation of Hydrogen−Deuterium Exchange Incorporation Factors from the Simulation Trajectory. Hydrogen−deuterium exchange incorporation factors (D_0^i) were calculated for all residues of apoA1 using experimental data from overlapping apoA1 peptides of nascent HDL analyzed by H/D-MS/MS, as described in our previous publications (*12*, *13*). To calculate per residue D_0^i values for all snapshots extracted from the simulation trajectory of apoA1, we used the hydrogen−deuterium exchange methodology implemented in DEXANAL (*12*, *13*). This methodology was validated by previously applying it to a set of protein crystal structures with published NMR-derived H−D exchange rate constants (k_{xc}^i) and/or H/D-MS/MS-derived D_0 values for peptides (*13*). For the sake of completeness, we briefly describe here the theoretical formalism behind this methodology. DEXANAL uses experimentally measured D_0 values for overlapping peptides determined by H/D-MS/MS (in the case of apoA1 of rHDL, there was >95% coverage), and a molecular model to produce a set of H−D exchange probabilities (XP_i) that are used to predict per residue deuterium incorporation factors (D_0^i), residue unfolding equilibrium constants (K_u^i), and H−D exchange rate constants (k_{xc}^i). Gauging the difference between experimental and calculated D_0 values assesses the input model.

The H−D exchange rate constant, k_{xc}^i, for each residue *i* relates to the experimentally derived D_0^i and the exchange time, *t*, by the following equation:

$$-k_{xc}^i t = \ln(1 - D_0^i) \quad (1)$$

The residue unfolding equilibrium constant, K_u^i (the reciprocal of the NMR protection factor), is the ratio of k_{xc}^i and the intrinsic H−D exchange rate constant (k_{ch}^i) of individual residues in unstructured loops (*45*, *46*):

$$K_u^i = \frac{k_{xc}^i}{k_{ch}^i} \quad (2)$$

For an ensemble of protein conformations, XP_i defines the ratio of the number of protein molecules ($N_D{}^i$) where the

backbone amide H of residue *i* exchanged with D to the total number of molecules:

$$XP_i = \frac{N_D^i}{N_D^i + N_H^i} \quad (3)$$

For a single conformation (and not an ensemble), XP_i for each residue *i* can be calculated as the product of two quantities (RAI_i and BAI_i) encoding structural information about residue *i*'s size, chemical composition, and interactions with the rest of the system:

$$XP_i = RAI_i \times BAI_i \quad (4)$$

This basic equation incorporates information about the degree of protection (both local solvent accessibility and dynamics) of the backbone amide H of residue *i*. BAI_i and RAI_i are the backbone and residue accessibility/dynamics indices, respectively, with values between 0 and 1. The probability correction factor (PCF_i) is the ratio of the experimentally determined per residue deuterium incorporation factor ${D_0}^i$ (obtained by partitioning the experimentally measured D_0 for peptic peptides) and the calculated probability XP_i:

$$PCF_i = \frac{D_0^i}{XP_i} \quad (5)$$

PCF gauges the difference in protection to exchange of a backbone amide H atom in the molecular model with respect to the same H in the real structure and is used to refine the conformation of individual residues in the model (i.e., adjust the protection of amide H's). Indices BAI and RAI are calculated using an approach similar to COREX (*47*).

The BAI index is the ratio of the atomic (van der Waals) surface area of the backbone amide H atom in the model $[({A_H}^i)_{model}]$ to that in the random coil conformation $[({A_H}^i)_{rc}]$.

$$BAI_i = \frac{(A_H^i)_{model}}{(A_H^i)_{rc}} \exp[-c \sum_j (d_{HB} - d_{HB}^0)] \quad (6)$$

If the amide H is involved in hydrogen bonding, BAI is modified by an exponential term that includes the length of the hydrogen bond (d_{HB}).

The RAI_i index of residue *i* is the ratio of the solvent accessible surface area of the residue in the model $(A^i)_{model}$ to that in the random coil $(A^i)_{rc}$ conformation:

$$RAI_i = \frac{(A^i)_{model}}{(A^i)_{rc}} f_i^{PD} \quad (7)$$

RAI is modulated by a factor f_i^{PD} that takes into account the dynamics of the protein (*12*, *13*), present in experimental data but not included in a single frozen conformation.

Calculation of Patch Hydrophobicity and Solvent Accessible Surface Area (*SASA*). Patch hydrophobicity (PH) is a calculated per residue index based on the hydrophobic indices of amino acid residues that takes into account the local environment of the residue within the predicted three-dimensional structure (*48*). PH was determined for each amino acid residue by averaging the hydrophobic indices of neighboring residues (within 15 Å) located on the same side of protein, i.e., either inside (facing the lipid) or outside (facing the solvent) (*13*). PH is thus a normalized residue index of solvent accessibility in the range of zero to one that incorporates local structure and accounts for the fact that a hydrophobic residue exposed to solvent, when surrounded by mostly hydrophilic residues, destabilizes the local conformation of the protein to a lesser extent. The solvent accessible surface area (SASA) of the protein was calculated using MSMS (*49*) and was separated into hydrophobic and hydrophilic contributions based on the hydrophobic index of amino acid residues. The SASA exhibited by the acyl chains originates mainly from regions of acyl chains exposed to solvent (*50*) and to a lesser extent from the fact that acyl chains pack less densely than polar headgroups and protein (*51*). Inspection of the simulation box shows that no water molecule was found inside the lipid core.

RESULTS

apoA1 Retains a Superhelical Conformation during the Entire Simulation. Nascent rHDL in solution reached thermodynamic equilibrium [i.e., constant average total energy (*E*) (Figure 1A)] after a roughly 20−30 ns simulation. The average *T* of the system remained constant [300 K (Figure 1B)] during the entire simulation. Analysis of the root-mean-square displacement (rmsd) of the apoA1 backbone during simulation indicates that the most significant change in the conformation of apoA1 (i.e., the decrease in the pitch of the overall helix) takes place during the first 10 ns (domain C of Figure 2A), after which the rmsd reaches a plateau (domain D of Figure 2A). Figure 2B shows the change in solvent accessible surface area (SASA) calculated throughout the simulation. Most of the SASA of apoA1 (~80%) corresponds to solvent-exposed hydrophilic amino acid residues. It is evident that the proper orientation of apoA1 amphipathic chains during the simulation contributes to the thermodynamic stability of the HDL particle as confirmed by the minimal variation in E (Figure 1A).

The overall conformation of apoA1 chains and the changes that occur during the molecular dynamics trajectory are illustrated in panels C (first 10 ns) and D (from 10 to 60 ns) of Figure 2. During the first 10 ns of the simulation, there is a noticeable decrease in the length of the particle's main axis (from 171 to 111 Å) and an increase in the shorter dimension (from 73 to 85 Å), leading to a more spheroidal shape. There is very little change in the conformation of apoA1 after 10 ns, and the protein retains the overall helicity and conformational asymmetry during the more prolonged simulation (Figure 2D). Importantly, despite the change in the overall dimensions of the particle (from an elongated ellipsoid to a spheroid), the overall architecture of apoA1 remains unchanged. Namely, the protein retains (1) the overall helical conformation as proposed for the DSH model of nascent HDL, (2) the secondary structure (i.e., the same degree of α-helicity), and (3) a global conformational asymmetry (i.e., the two associated N- and C-termini fold back and interact with the rest of the protein distinctly). We hypothesize that this asymmetry of apoA1 proposed for the first time in the DSH model is characteristic of nascent HDL and is reflected in several structural features of the protein conformation, which will be discussed later (vide infra).

Simulation Confirms That the Micellar and Pseudolamellar Organization of Lipids in Nascent HDL Is Thermodynamically Stable. Like the analysis of apoA1 trajectory, Figure 3A shows the superposition of various models of the lipid phase (POPC and cholesterol) corresponding to simulation snapshots. The left panel displays the superposition of 11 snapshots taken in the first 10 ns of simulation, while the right panel shows the superposition of 11 snapshots taken during the next 50 ns. While the change in shape from prolate ellipsoid to

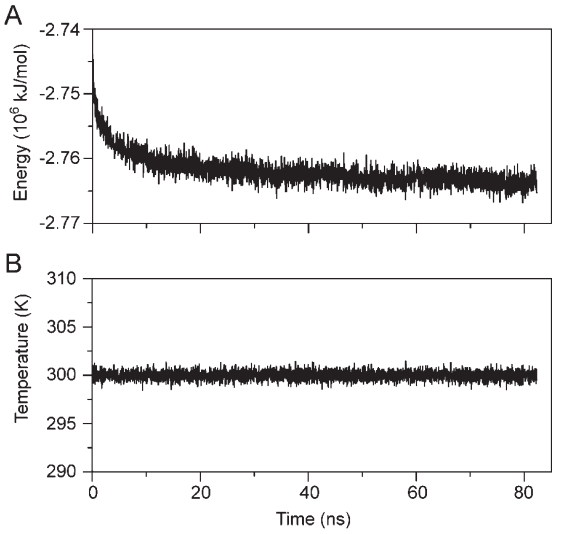

FIGURE 1: Energy and temperature fluctuations during the molecular dynamic simulation of nascent HDL in solution. (A) Fluctuation in the total potential energy of the simulation cell. The graph shows that it takes ~30 ns simulation for the system to reach thermodynamic equilibrium. (B) Fluctuation in the absolute temperature. The system maintains on average the temperature setup for simulation (300 K).

spheroid is visible during the first 10 ns, it is worth noting that the overall lipid organization (micellar and pseudolamellar packing) proposed for the DSH model of nascent HDL is retained during this part of the simulation, and the lipid remains in the proper orientation with respect to solvent; i.e., polar headgroups are oriented outward (toward solvent), while acyl chains are oriented inward (toward each other) and toward the hydrophobic surfaces of apoA1.

Analyses of SASA during the trajectory of the simulation confirm that the lipid polar headgroups and hydroxyl group of cholesterol contribute the most to SASA (Figure 3B). The fact that the major contribution to solvent accessible surface comes from lipid polar headgroups and is retained during simulation indicates that the micellar and pseudolamellar organization of the lipid in nascent HDL is thermodynamically stable when it is bound to protein. The left panel of Figure 3C shows the overall structure of the lipid core after a 60 ns simulation (polar headgroups colored purple and fatty acyl chains green). The visible diagonal green stripe on the lipid surface corresponds to the place where the antiparallel apoA1 chains are located in the model. The right panel displays a cross section through the HDL particle, which reveals the micellar and pseudolamellar packing of the lipid with polar headgroups pointing radially outward, and acyl chains and the sterol core of cholesterol pointing inward. The protein chains are visible at the periphery of the particle, and cholesterol molecules are shown to intertwine with the acyl chains.

A noticeable feature of the simulated lipid phase is the presence of a central empty cavity. Inspection of the simulation box shows that no solvent molecule penetrated the lipid layer, and the cavity is empty (i.e., free of solvent). It is noteworthy that previous experimental scattering studies of micellar systems have shown the existence of a central void within micellar systems (*52*, *53*), and molecular dynamics simulations of micellar systems have similarly predicted the presence of such voids (*51*, *54*, *55*), with ellipsoidal to spheroidal shape changes depending upon subtle changes in the molecular dynamics force fields used (*56*, *57*). Prior molecular dynamic simulations of micellar systems (*56*, *57*) suggest that the change in shape may be attributed to an imbalance between polar interactions among polar headgroups of the lipid, on the one hand, and dispersion interactions among acyl chains, on the other (vide infra).

The ^{31}P NMR Chemical Shift and Half-Line Width of POPC Point to Micellar Packing of Lipids in Nascent HDL. The micellar organization of lipids posited in the DSH model of HDL and the molecular dynamics simulation studies presented here suggests a highly dynamic environment for the phospholipids within rHDL. We therefore sought to perform experimental studies to directly address this possibility. Prior studies have shown that ^{31}P NMR of the polar headgroup phosphate moiety of phospholipids can distinguish between different smectic mesophases (molecular packing arrangements) because lamellar, micellar, and hexagonal array arrangements of phospholipids demonstrate distinct ^{31}P NMR spectral features, including distinct chemical shifts, line shapes (symmetric vs asymmetric with upfield or downfield tails), and line widths (*33*, *35*, *58*, *59*). ^{31}P NMR analyses of both nascent rHDL and pHDL demonstrate a sharp isotropic peak at 0 ppm (Figure 3D and inset). The chemical shift, line width, and symmetrical shape are all consistent with a micellar smectic mesophase (*33*, *35*, *58*).

While the chemical shift of the ^{31}P NMR spectra for HDL preparations indicates a micellar and nonlamellar organization, a small particle rapidly tumbling in all orientations could theoretically contribute to the isotropic spectral features observed for both pHDL and rHDL. We therefore compared the ^{31}P NMR half-line width of the phospholipid within HDL with the spectral characteristics of phosphate within SUV of differing sizes. SUV with different radii (measured with dynamic light scattering) were made with the most abundant phosphatidylcholine molecular species present within rHDL and pHDL (POPC) by passage of the lipid multiple times through different extrusion pore sizes (Materials and Methods). POPC was chosen for the generation of SUV of varying radii because it is known to have a strong lamellar phase packing preference as demonstrated by X-ray diffraction (*34*). The line widths (in hertz) at half-peak height observed during ^{31}P NMR analyses of each vesicle preparation and both rHDL and pHDL are shown in Figure 3D. As expected, a linear relationship (R = 0.98) was observed between the particle radius and ^{31}P NMR line width for varying sized SUV (Figure 3D). Upon extrapolation to the half-line width predicted for a vesicle (bilayer lipid packing) the same size of a nascent HDL particle (radius of gyration of 51.3 Å), the half-line width predicted for a lamellar phase particle is considerably larger than that observed with either rHDL or pHDL (Figure 3D). Collectively, these results demonstrate that the environment experienced by the phosphate group of the phospholipid within HDL is highly dynamic with greater isotropic motion than what would be observed with a similar sized bilayer (SUV) organized particle.

Repeat Small Angle Neutron Scattering and Electron Microscopy Studies Visualize Nascent HDL as a Prolate Ellipsoid. The shape of the HDL particle during simulation changes from elongated ellipsoid, as proposed in the DSH model (*13*), to spheroid. This is the only simulation result that differs from experimental evidence, with all other features of SANS and other biophysical platforms (as outlined below) matching the simulation results. This was surprising because the prolate ellipsoid shape of the DSH model is based upon experimental observation, i.e., direct visualization of the particle by small angle neutron scattering (SANS) and electron microscopy (EM) (*13*).

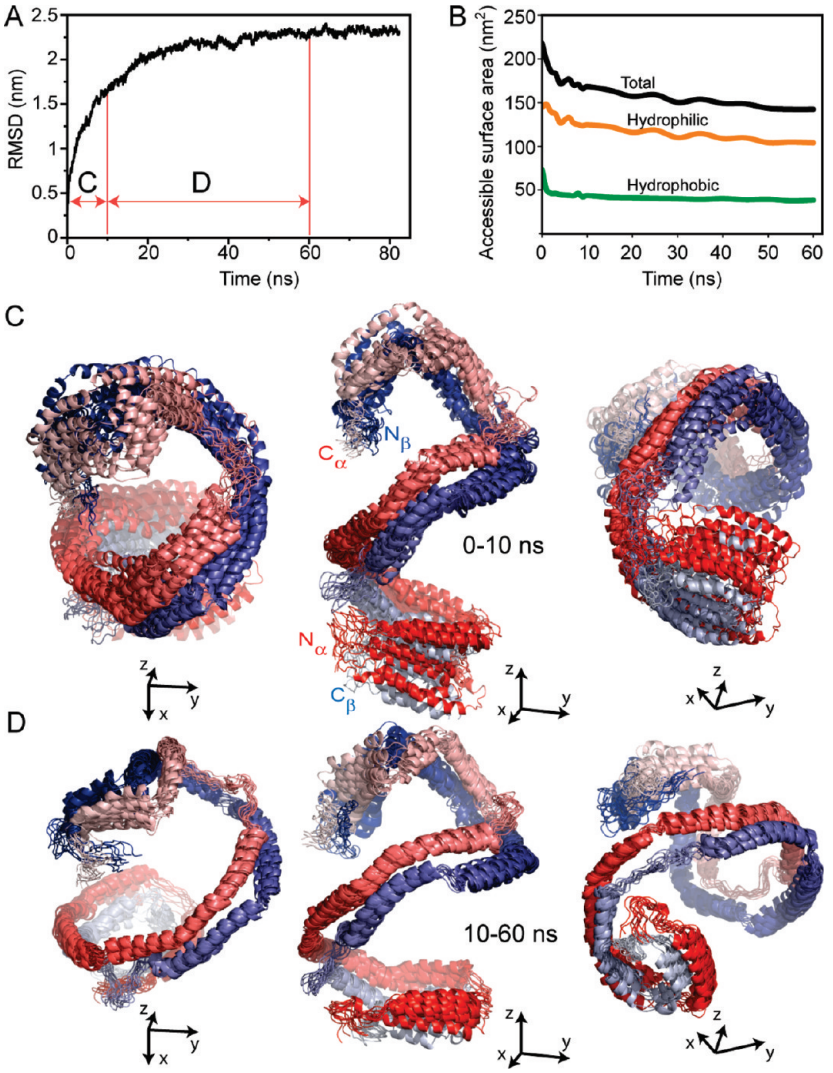

FIGURE 2: Root-mean-square displacement (rmsd) of the apoA1 backbone from the conformation of apoA1 in the Double Super Helix model of nascent HDL. (A) Fluctuation in the rmsd of the apoA1 backbone conformation during simulation. The graph shows that most of the conformational change in the apoA1 backbone occurs in the first 10 ns of simulation. (B) Change in the total (black), hydrophilic (orange), and hydrophobic (green) solvent accessible surface area (SASA) of apoA1 during simulation. Most of the solvent accessible surface of apoA1 (~80%) is made of hydrophilic amino acid residues. (C) Superposition of 11 simulation snapshots taken 1 ns apart during the first 10 ns. apoA1 chains are colored from N to C terminus with a gradient from dark red to light red or dark blue to light blue with the N-termini colored dark red and dark blue and C-termini colored light red and light blue. The left and right panels show the same superposition of frames from different vantage points with the N-terminus of chain A pointing outward in the left panel and the N-terminus of chain B pointing outward in the right panel. (D) Conformational changes in the apoA1 backbone during the next 50 ns simulation. The three panes confirm the result in panel A; that is, there is little change in the conformation of the apoA1 backbone after the first 10 ns simulation. In the left and right panels, the N- and C-terminal pairs of apoA1 point outward, emphasizing the helical shape of apoA1, which is retained during the entire simulation.

To experimentally reassess the global shape of rHDL, new SANS experiments with contrast variation were performed. The experimental scattering data and predicted scattering curve for the protein (at 12% contrast) and lipid (at 42% contrast) are shown in Figure 1 of the Supporting Information. Comparison of the low-resolution structures of protein and lipid components of rHDL from the original SANS studies used for generation of the DSH model (Figure 4A) and the new SANS shapes for protein and lipid obtained from experiments on new rHDL preparations (Figure 4B) reveals striking similarity. The shape of the protein has the same spatial characteristics, i.e., a helix that wraps around a prolate ellipsoid lipid core. In addition, EM micrograph analyses of rHDL preparations (Figure 4C) confirm that the rHDL particles are elongated ellipsoids of ~165−170 Å, in close agreement with the overall dimensions of the ellipsoid obtained from independent sets of SANS analyses. We conclude from the direct experimental observations using both SANS and EM that the overall shape of rHDL is a prolate ellipsoid.

Further comparison of experimental SANS data, obtained from samples examined at 12% D_2O contrast, with theoretical results derived from simulation is illustrated in Figure 5, along with the change in apoA1 shape and of the overall HDL particle during the course of simulation from an elongated ellipsoid [DSH model (Figure 5A)] to a spheroid [60 ns (Figure 5B)]. During the simulation, the radius of gyration (R_g) decreases from 52.3 to ~44 Å, with the majority of the change in R_g occurring during the first 10 ns of the simulation (Figure 5C). A comparison of the experimental and calculated SANS scattering intensities during the molecular dynamics trajectory is shown in Figure 5D. The predicted scattering intensities of various simulation-derived models show that the scattering curves depart from the experimental data as the simulation progresses, and the departure

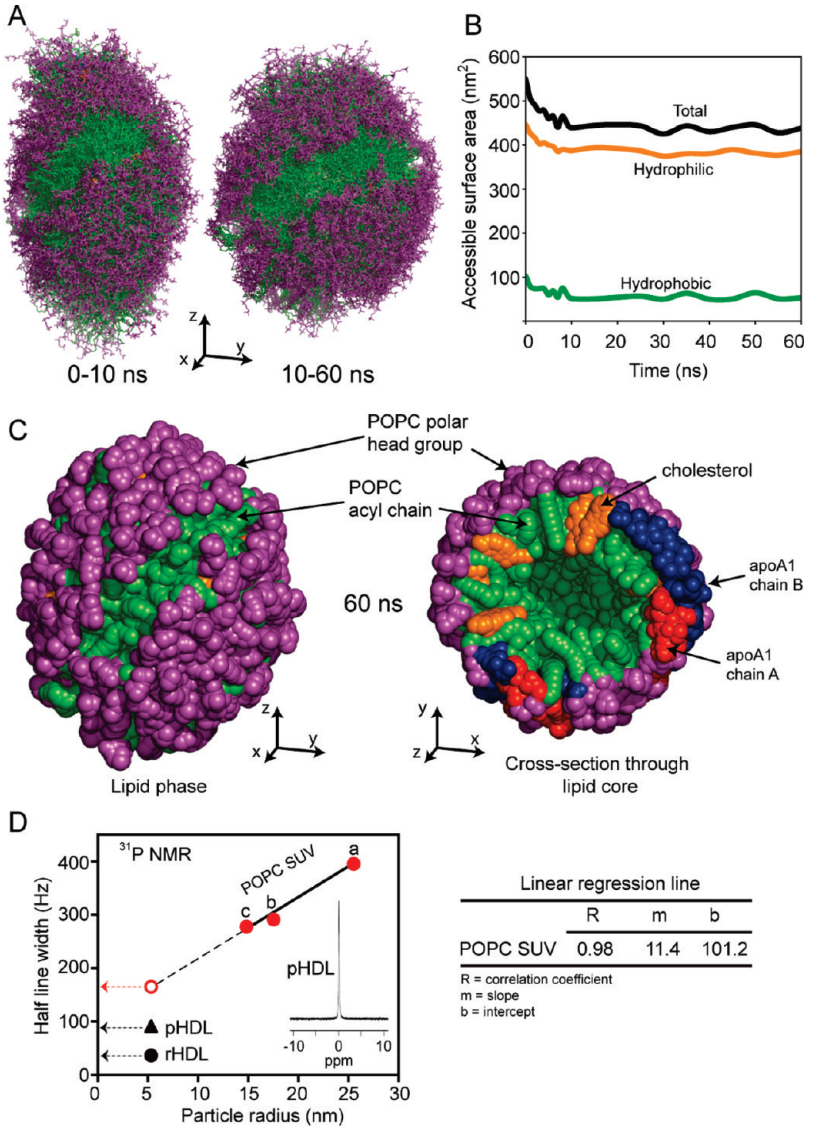

FIGURE 3: Simulation trajectory of the lipid phase component of nascent HDL. (A) The left panel shows the superposition of 11 snapshots taken during the first 10 ns simulation. The polar headgroups of POPC are colored purple and the acyl chains green. Cholesterol is colored orange. The right panel shows the superposition of 11 snapshots taken during simulation in the next 50 ns (from 10 to 60 ns). The superposition shows that the lipid core becomes more spheroidal and that the most significant change in its shape takes place during the first 10 ns. (B) Changes in the hydrophobic (green), hydrophilic (orange), and total (black) solvent accessible surface area during simulation. (C) The left panel shows the packing of the lipid core after a 60 ns simulation. The polar heads of POPC are shown as purple beads, while the acyl chains are shown as green beads. Cholesterol molecules are colored orange. The right panel shows a cross section through the lipid core and apoA1 double chain (red and blue). The panel shows the micellar−lamellar structure of the lipid core with the POPC polar headgroups oriented radially toward solvent and acyl chains pointing inside. (D) Plot of the half-line width of the ^{31}P NMR spectrum recorded for multiple distinct small unilamellar vesicles (SUV) of differing size produced from POPC, reconstituted HDL (rHDL), and nascent HDL isolated from human plasma (pHDL). SUV with diameters of >20 nm were generated by sequential extrusion through polycarbonate filters with 0.4, 0.1, 0.05, and 0.03 mm pore sizes 15 times. POPC SUV with a diameter of 17.6 nm were generated in a manner similar to that for POPC SUV with a diameter of 25.6 nm, but with 30 extrusions. POPC SUV with a diameter of 14.9 nm were generated using the cholate dialysis method.

correlates with the change in the R_g of the model. In addition, the scattering curves for the simulation models develop humps, which become accentuated as the simulation progresses. Figure 5E displays the goodness of fit (χ^2) of experimental versus calculated intensities for various simulation models during the course of the molecular simulation. It is worth noting that during the first 30 ns the goodness of fit deteriorates monotonically and then starts oscillating, an indication that apoA1 starts changing conformation back to some extent. For example, the models obtained after 30 and 60 ns have the same χ^2.

The H−D Exchange Predicted from the Simulation Agrees with Experimental Data. The analysis of the fluctuations in apoA1 backbone amide H−D exchange rate constants (k_{ex}), deuterium incorporation factors (D_0), and per residue unfolding constants (K_u) during the course of the simulation indicates that the average D_0 values predicted from simulation are consistent with experimental data (Figure 6 and Table 1 of the Supporting Information). Comparisons of experimental and predicted D_0 values, correlation coefficients (R), and patch hydrophobicities (PH) for 0−10 and 10−60 ns trajectories are also shown (Figure 6). Notably, the trajectory analyses show D_0 and R in close agreement with the same experimental quantities, and that the partition of the amino acid residues (based on PH made in the DSH model) is retained during the entire simulation. The overall goodness of fit of the experimental H−D exchange data derived from analysis of rHDL and the calculated H−D

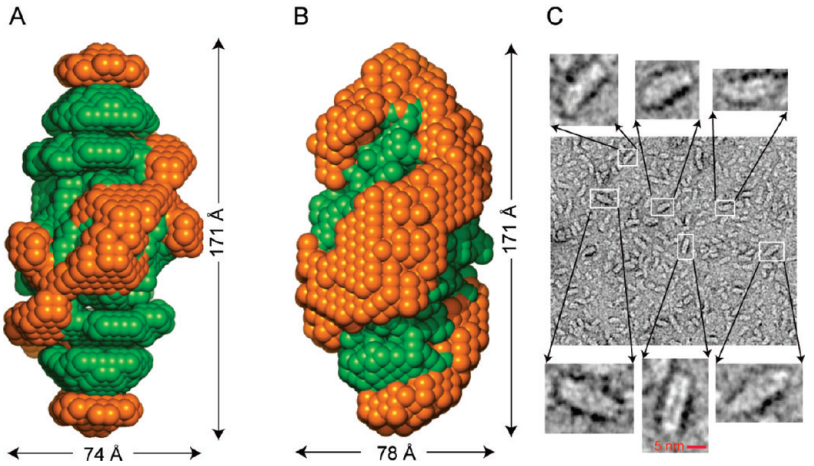

FIGURE 4: Low-resolution structures of nascent HDL from small angle neutron scattering (SANS) and images from electron microscopy: (A) Superposition of SANS low-resolution structures of apoA1 (orange) and the lipid core (green) of nascent HDL obtained from processing scattering intensities collected at Intitut Laue-Langevin in Grenoble, France, as previously reported (*13*). (B) Repeat low-resolution structures for protein and lipid within rHDL preparations obtained from data collected at JCNS, Garshing, Germany, during this study. (C) Electron microscopy micrograph of rHDL preparations. Detailed magnified insets show that the majority of the particles are prolate ellipsoids.

exchange data for the starting DSH model and molecular dynamics simulation models of nascent HDL are shown in Table 1. Both the correlation between the experimental and theoretical H−D exchange incorporation factors of peptic peptides (D_0) and the rmsd of the difference between the experimental H−D exchange data and the calculated ones show excellent agreement throughout the course of the simulation.

A residue level analysis of the H−D exchange data and the correlation with PH of individual residues is shown for the entire particle in Figure 7, and for two distinct regions of the lipoprotein in Figures 8 and 9. Figure 7A displays a combination of average per residue PH (top stripe) and both simulated and experimentally derived per residue $D_0{}^i$ (graphs below) for apoA1. Data for the 0−60 ns simulation shown are the maximum (orange), minimum (green), and mean (black dotted) calculated $D_0{}^i$ values plotted versus residue number, with superimposed experimentally determined $D_0{}^i$ (solid line) from H/D-MS/MS analyses of rHDL. All values show remarkable periodicity that correlates with the secondary structure of the protein (vide infra). Figure 7B displays the 60 ns trajectory of apoA1 made of all 21 snapshots (see Materials and Methods), and the overlaid snapshots show that most hydrophilic residues (in terms of PH, colored orange) are exposed to solvent and the majority of hydrophobic residues (in terms of PH, colored green) face inward where they are in contact with the lipid. This also points to the fact that the hydrophilic−hydrophobic partition of apoA1 residues proposed in the DSH model produces a thermodynamically stable structure.

In further analyses, we investigated the relation between the secondary structure of apoA1 and the observed periodicity of H−D exchange data by performing separate analyses of H−D exchange and PH on domains of apoA1 with distinct secondary structure (i.e., either α-helical or random coil loop). For example, Figure 8 displays the results of the analysis performed on a predominantly α-helical domain of apoA1 (Tyr_{100}−His_{155}) that hosts what has historically been called helix h_4 (Pro_{99}−Glu_{120}), h_5 (Pro_{121}−Ser_{142}), and part of h_6 (Pro_{143}−Ala_{164}). Simulation results shown in Figure 8B reveal that this domain of apoA1 remains α-helical during the entire trajectory. The top graph of Figure 8A displays oscillations in the experimental (solid line) and simulation-derived $D_0{}^i$ (maximum, minimum, and average simulation data shown as orange, green, and black dotted lines, respectively). The PH for individual residues is shown in the top stripe. For example, in HDL models extracted from simulation snapshots, both Ala_{152} residues (both chains of apoA1) are predicted to face the lipid core and are predicted to be involved in hydrogen bonding. Amide H of Ala_{152A} persists in hydrogen bonding 100% of the simulation; H of Ala_{152B} persists 90%. The experimentally derived $D_0{}^i$ values for these amino acid residues are 0.05 (chain A) and 0.04 (chain B), and the average, minimum, and maximum values of the predicted $D_0{}^i$ agree well with the former (0.04, 0.03, and 0.05 for chain A and 0.05, 0.03, and 0.24 for chain B, respectively). Thus, both experimental and simulation results indicate that the Ala_{152} residues of both apoA1 chains experience minimal hydrogen−deuterium exchange, and minimal dynamics. In contrast, the Ser_{142} residues of both apoA1 chains face the solvent. Amide H of Ser_{142A} is involved in hydrogen bonding only 24% of the simulation, while H of Ser_{142B} persists 67%. The experimentally derived $D_0{}^i$ values for these amino acid residues are 0.97 (chain A) and 0.93 (chain B). The average, minimum, and maximum values of predicted $D_0{}^i$ are 0.86, 0.53, and 1.00 for chain A and 0.83, 0.55, and 1.00 for chain B, respectively. The average values for both chains (0.86 and 0.83) are in reasonable agreement with the experimental $D_0{}^i$ (0.97 and 0.93). The experimental and simulation-predicted $D_0{}^i$ values for Ser_{142} are congruent and show that the amide proton on this residue rapidly exchanges with solvent and experiences much more dynamics than Ala_{152}. It is also interesting to note that even though some of the residues in apoA1 are extremely dynamic with a large range of predicted $D_0{}^i$ values, there is remarkable concordance between the predicted average $D_0{}^i$ across the simulation trajectory (dotted line, Figure 8A) and the experimental $D_0{}^i$ derived from H/D-MS/MS analyses (solid line, Figure 8A).

The marked oscillatory behavior of the experimental and simulation-derived per residue deuterium incorporation factors, $D_0{}^i$, is consistent with the predominantly α-helical secondary structure and lipid interfacial environment of apoA1. Thus, while in globular proteins hydrogen bonding can play a dominant role in the overall rates of H−D exchange of amide protons (*60*), in

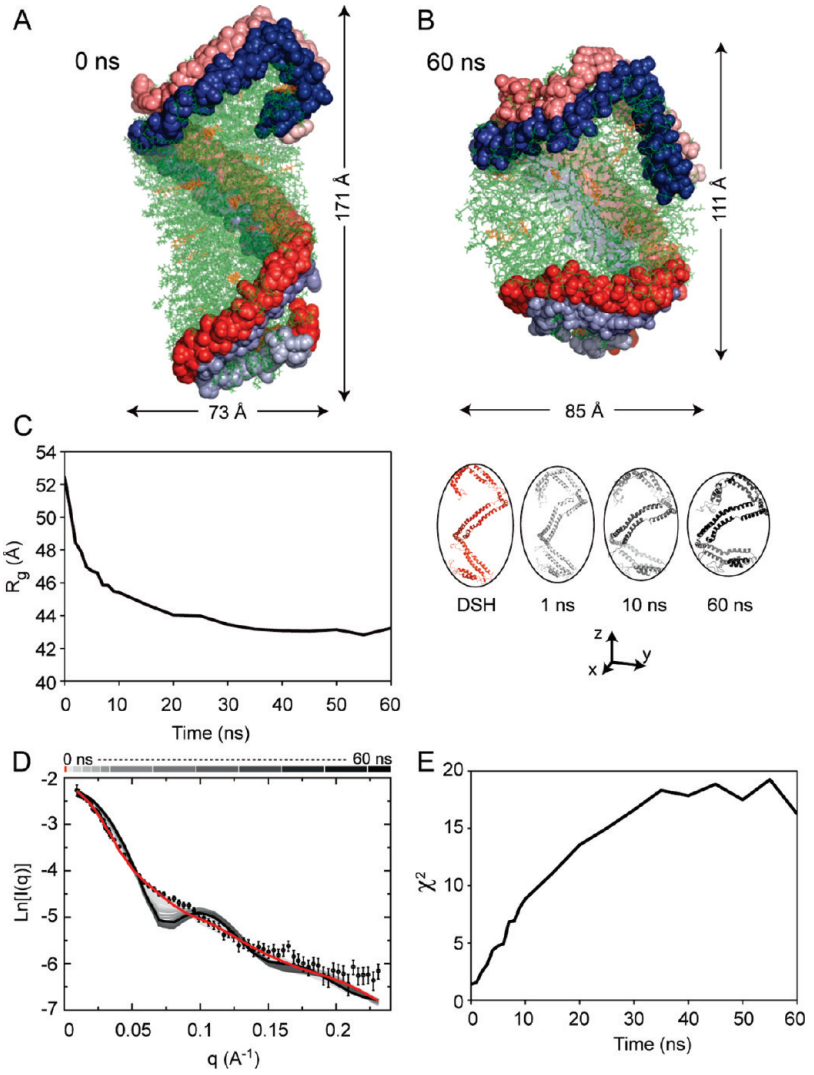

FIGURE 5: Comparison of experimental and calculated small angle neutron scattering (SANS) intensities for the Double Super Helix (DSH) model of nascent HDL, and models obtained during the 60 ns simulation. (A) DSH model of nascent HDL in which apoA1 is represented with spheres with the two chains are colored red and blue fading from the N- to C-terminus. The phospholipid is colored green and free cholesterol orange. (B) Model of nascent HDL obtained from the simulation after 60 ns. (C) The left panels shows the radius of gyration (R_g) during the simulation trajectory. The right panel shows the conformations of apoA1 (cartoon representation) in the DSH model (red) and after simulation for 1, 10, and 60 ns. (D) Comparison of the experimental scattering intensity (empty circles with error bars) with those obtained by calculation from the DSH model (red line) and all 21 snapshots during the simulation trajectory (various shades of gray). The gray bar at the top of the graph color codes the intensity curves: light gray for conformations of apoA1 at the beginning of the simulation and dark gray for the conformation toward the end of the simulation. The intensity line corresponding to the last simulation snapshot (60 ns) is colored black. (E) χ^2 statistics, which gauge goodness of fit between the experimental and theoretical intensities, as a function of simulation time. $\chi^2 = 1.37$ for the DSH model.

HDL, the lipid environment has a dramatic impact on the overall H−D exchange in apoA1 amide hydrogens. Figure 8B displays a superposition of the models of apoA1 corresponding to the 0−60 ns trajectory. The superposition of these apoA1 domain models shows that "patch" hydrophilic residues (orange) remain solvent-exposed (left panel) while patch hydrophobic residues (green) remain buried during the simulation, facing the lipid core.

A similar analysis was performed for the loop domain of His_{155}−Arg_{177} (Solar Flare, SF) of apoA1 chains A and B and is shown in Figure 9. These loops host part of helices h_6 (Pro_{143}−Ala_{164}) and h_7 (Pro_{165}−Gly_{186}). Figure 9A displays graphs with changes in experimental and simulation-predicted D_0^i values, and the PH on the top stripes. A notable feature of this region of apoA1 within rHDL is that the variation in D_0^i values does not follow the same oscillatory pattern as in the case of predominantly α-helical domains (e.g., Figure 8). Most residues in the SF loops show markedly rapid H−D exchange rates and have corresponding enhanced predicted dynamics exemplified by the range of predicted D_0^i, k_{xc}^i, and K_u^i values (Table 1 of the Supporting Information). Some residues within the SF loops exhibit markedly dynamic character. For the sake of clarity, Figure 9B shows the superposition of 11 snapshots only (every 5 ns between the 10 and 60 ns simulation trajectory) of these loop domains of apoA1 in rHDL. The PH is displayed in the stripes on top of the graphs and color coded in the models. Visual inspection shows that the majority of the residues in the SF region remain as protruding solvent-exposed loops during the entire simulation, consistent with the experimental H−D data. These findings support the idea that these loops are thermodynamically stable structures that remain highly exposed to solution.

Simulation Models Preserve the Experimental Distance Constraints and Overall Asymmetry of the apoA1 Shape Proposed for the DSH Model. A wealth of experimental

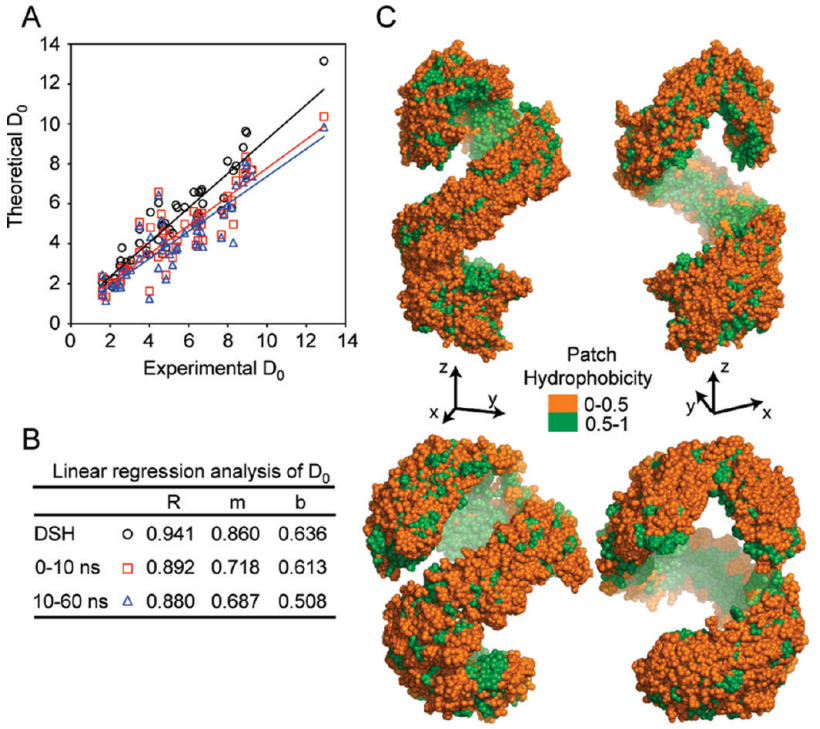

FIGURE 6: Comparison between experimental and calculated deuterium incorporation factors (D_0) using molecular dynamics trajectory snapshots. (A) Experimental vs theoretical D_0 values and regression lines corresponding to the Double Super Helix model (black, empty circle), the average over 11 snapshots in the first 10 ns (red, empty square), and average over 11 snapshots between 10 and 60 ns (blue, empty triangle). (B) Correlation coefficients (R) between experimental and theoretical D_0 values and slope (m) and intercept (b) of the linear regression lines for the D_0 values. (C) The top panel shows the patch hydrophobicity of apoA1 in nascent HDL from simulation frames in the range of 0−10 ns. The hydrophilic surface is colored orange and the hydrophobic surface green. The bottom panel shows the patch hydrophobicity of apoA1 in nascent HDL from simulation frames in the range of 10−60 ns.

Table 1: Goodness of Fit between Experimental Hydrogen−Deuterium Exchange Data and the Calculated Hydrogen−Deuterium Exchange Data for the Double Super Helix and Molecular Dynamics Simulation Models of Nascent HDL

model	correlation coefficient[a]	rmsd[b]
Double Super Helix	0.946	0.82
0−10 ns[c]	0.892	1.47
10−60 ns[d]	0.880	1.70
0−60 ns[e]	0.888	1.56

[a]Correlation between the theoretical hydrogen−deuterium exchange incorporation factors of peptic peptides (D_0) in the DSH or simulation model and the actual experimentally measured deuterium incorporation within apoA1 peptic peptides. [b]Root-mean-square deviation, which quantifies the difference between the experimental hydrogen−deuterium exchange data and the calculated ones. A smaller rmsd indicates a better agreement between experiment and theory. [c]Eleven snapshots in the range of 0−10 ns separated by 1 ns were used to perform H/D-MS/MS calculations and average over all the snapshots. [d]Eleven snapshots in the range of 10−60 ns separated by 5 ns were used to perform H/D-MS/MS calculations and average over all the snapshots. [e]Twenty-one snapshots in the range of 0−60 ns were used to perform H/D-MS/MS calculations and average over all the snapshots.

investigations (FRET, MS/MS cross-linking, and ESR) report various distance constraints in apoA1 of rHDL (*9*, *11*, *61*−*63*). We therefore analyzed the simulation models for goodness of fit with available reported distance constraints from diverse biophysical approaches. Remarkably, we found that during the trajectory of the simulation, virtually all distance constraints can be accommodated. Table 2 lists the distance constraints obtained from the different experimental platforms, together with those found in the DSH model. Also shown are predicted minimum, average, and maximum values of the constraints obtained from simulation by the analysis of the simulation trajectory. The distance constraints listed for the DSH model incorporate specific modifications of amino acid residues according to the biophysical method used for their determination. For example, to compare distance constraints from the DSH model with those obtained from FRET experiments (*11*), the distance was measured between a Trp residue and a residue modified in silico to cysteine and attachment of the AEDANS acceptor (covalent adduct with 5-{2-[(1-oxoethyl)amino]ethylamino}-1-naphthalenesulfonic acid). When ESR data were used (*9*), both residues were modified to cysteine and the methane thiosulfonate nitroxide spin-label (MTSSL) probe was attached. To compare with distance constraints obtained from MS/MS cross-linking (*9*, *61*−*63*), in the DSH model we freely rotated the lysine residue to obtain the minimum distance between them. None of these transformations have been applied to models produced from simulation because it was impractical to do this for such a large number of structures. Thus, the distances obtained from simulation models are between the extremities of nonmodified amino acid residues involved in the distance constraints and underestimate the distances that would be observed with the probes covalently attached for the FRET and ESR studies. The additional transformations on residues that we performed for the DSH model in principle lead to a decrease in the distance between residues because the AEDANS and MTSSL attachments are rather large (15 and 6.5 Å, respectively). Thus, if the distance between residue extremities in simulation models is close (e.g., <40 Å) to the experimental constraint, then the attachment of the AEDANS or MTSSL probes will bring the experimental and theoretical constraints into agreement.

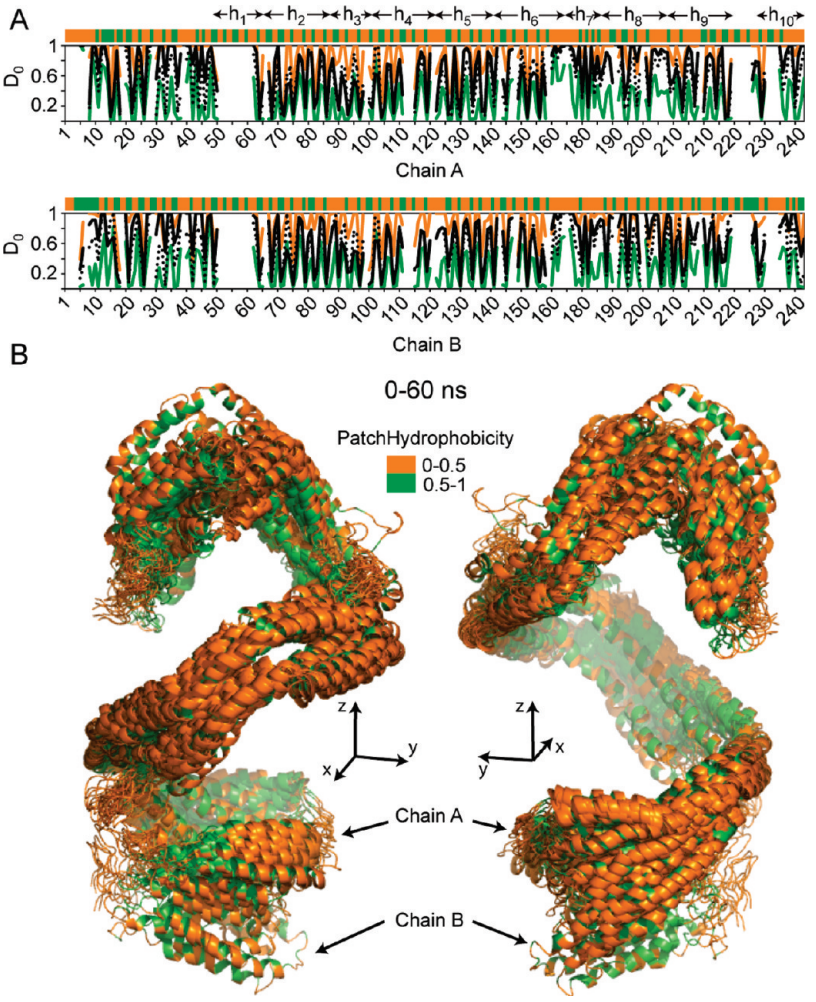

FIGURE 7: Hydrogen−deuterium exchange incorporation factors (D_0) and patch hydrophobicity of full-length apoA1 in nascent HDL. (A) The top panel shows patch hydrophobicity (top orange/green stripe) and a comparison between experimental (black line) and calculated D_0 values for residues of apoA1 chain A. The orange and green lines identify the maximum and minimum, respectively, of the D_0 range of fluctuations calculated from simulation snapshots. The black dotted line represents the average of calculated D_0 values obtained from all 21 snapshots taken during the first 60 ns simulation and used for analysis. On top of the patch hydrophobicity stripe the traditional α-helix domains on apoA1 (h_1−h_{10}) are identified. The bottom panel shows similar information for residues in chain B of apoA1. These two plots show that the average D_0 obtained from simulation follows the same pattern as the experimentally derived D_0. (B) Superposition of all 21 snapshots of apoA1 (chains A and B) taken during first 60 ns simulation. The apoA1 chains are shown in cartoon representation. The residues are colored according to their patch hydrophobicity (orange for solvent accessible residues and green for buried residues). Left and right panels show the trajectory of apoA1 in two different orientations. In the left panel, helix 5 is facing the viewer, while in the right panel, helix 5 is facing away from the viewer.

As shown in Table 2, all distance constraints satisfied in the DSH model are also satisfied in the simulation models. In addition, there are a couple of intrachain MS/MS cross-linking constraints not satisfied in the DSH model (K_{88}−K_{118} and K_{96}−K_{118}) that have minimum distances much shorter in simulation models (K_{88}−K_{118}, 69.1 → 27.9 Å; K_{96}−K_{118}, 64.2 → 37.9 Å). Another interesting aspect is the fact that the analysis of distance constraints points to a lack of symmetry in constraints between protein chains. For example, the constraint between K_{12A} and K_{182B} (minimum of 15.9 Å) is not detected between K_{12B} and K_{182A} (minimum of 50.1 Å). These situations highlight the prediction that the conformations of the two chains of apoA1 within rHDL are dissimilar.

The Solar Flare Loops Remain Solvent Accessible and Do Not Collapse during the Simulation. The original application of H−D exchange to the study of rHDL resulted in identification of an unusual region of apoA1 demonstrating a particularly rapid rate of H−D exchange, consistent with highly solvent exposed protruding loops named the Solar Flares (*12*). Experimental studies involving apoA1 mutagenesis and peptide competition binding studies confirmed this region corresponded to an LCAT interaction site, facilitating LCAT activation (*12*). In the DSH model of nascent rHDL, the Solar Flare loops are proposed to be retained, with charged residues (Arg_{160}, His_{162}, and Asp_{168}) of apoA1 forming a pair of salt bridges. Despite the experimental data demonstrating marked H−D exchange and the subsequent functional studies, the presence of stable Solar Flare loops has been debated. Using only a computational approach, Shih et al. (*64*) reported a brief 1 ns simulation and suggested the SFs "collapse" because a salt bridge within the SF was not preserved throughout the simulation (*64*). In our studies, we therefore conducted more in-depth analyses of the SF regions, including analysis of the formation and cleavage of predicted salt bridges (e.g., Arg_{160}−Asp_{168}−His_{162}) in the Solar Flare loops during simulation. The graph in Figure 10A displays the change in predicted distance (nanometers) between the charged residues involved in the ternary salt bridges during the course of the simulation (i.e., Arg_{160}−Asp_{168} and His_{162}−Asp_{168} in both chains of apoA1; red for chain A and blue for chain B). This analysis shows that the His_{162}−Asp_{168} salt bridge persists during

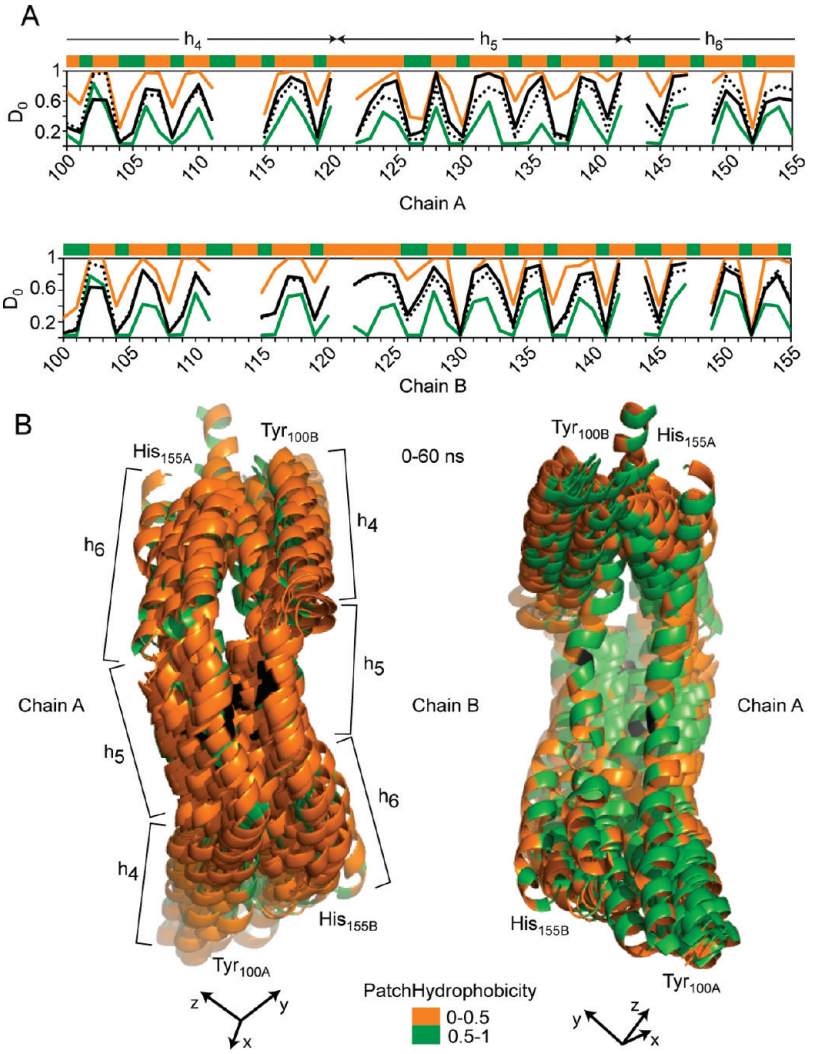

FIGURE 8: Hydrogen−deuterium exchange incorporation factors (D_0) and patch hydrophobicity in an α-helical region of apoA1 (Y_{100}−H_{155}) that hosts helix h_4 (P_{99}−E_{120}), helix h_5 (P_{121}−S_{142}), and part of helix h_6 (P_{143}−A_{164}). (A) The top panel shows patch hydrophobicity (top stripe) and a comparison between experimental (black line) and calculated D_0 values for residues in the Tyr_{100}−His_{155} region of apoA1 chain A. The orange and green lines identify the maximum and minimum, respectively, for the range of fluctuations of D_0 values calculated from simulation snapshots. The black dotted line shows the average value of calculated D_0 obtained from all 21 snapshots taken during the 60 ns simulation and used for analysis. The bottom panel shows similar information for the Tyr_{100}−His_{155} region of chain B of apoA1. These two plots show that the average values of D_0 obtained from the simulation follow the same pattern as the experimentally derived D_0 values and agree well with the latter. (B) Superposition of all 21 snapshots of the Tyr_{100}−His_{155} region (chains A and B) taken during the 60 ns simulation. The apoA1 chains are shown in cartoon representation, indicating that this region of the protein maintains α-helix secondary structure during the entire simulation. The residues are colored according to their patch hydrophobicity (orange for solvent accessible residues and green for buried residues). h_5 of apoA1 is facing upward (out of the page) because of the curvature of the apoA1 chains. As a reference point, Gly_{129}, the middle point of h_5, is colored black. The left and right panels show the trajectory of the Tyr_{100}−His_{155} region in different orientations. The left panel shows the trajectory having the solvent accessible surface (orange) of residues facing the viewer, while the right panel shows the trajectory with the buried residue surface (green) facing the viewer. h_5 is facing away from the viewer (into the page).

the entire simulation in both chains, while the Arg_{160}−Asp_{168} salt bridge in chain A breaks after approximately 3 ns. Of note, the latter salt bridge is predicted to again be re-formed briefly at the ~50 ns point of simulation. On the other hand, the salt bridge made of the same residues located on chain B (Arg_{160B}−Asp_{168B}) is predicted to persist over the entire simulation. The analysis of salt bridge dynamics in the SF loops confirms that salt bridges are not irreversible covalent bonds but, rather, are ephemeral and may be broken and remade during simulation. Importantly, these domains retain their overall solvent-exposed conformation (Figure 10) regardless the fate of the salt bridges.

Salt Bridges Provide Stability to the apoA1 Chains That Serve as a Backbone for the HDL Particle. The persistence of salt bridges over the course of the molecular dynamics simulation can give insights into structures of potential importance in HDL function. We therefore monitored salt bridge formation and cleavage throughout the particle during the simulation and analyzed the stability and dynamics of interchain salt bridges in terms of persistence over the trajectory. Figure 11 displays the location and persistence (in gray scale) of the interchain salt bridges on the apoA1 dimer identified during the simulation. The salt bridges are displayed on the conformation of apoA1 present at the beginning of the simulation. Table 3 provides the minimum, maximum, and average distances between charged residues for each salt bridge identified during simulation and its persistence. There are 25 interchain salt bridges predicted to be located in the N_α/C_β half-domain of the apoA1 dimer and 22 predicted to reside in the other half-domain (N_β/C_α) during the course of the entire simulation. Of note, only seven salt bridges in the N_α/C_β half-domain and two in the N_β/C_α half-domain were observed to

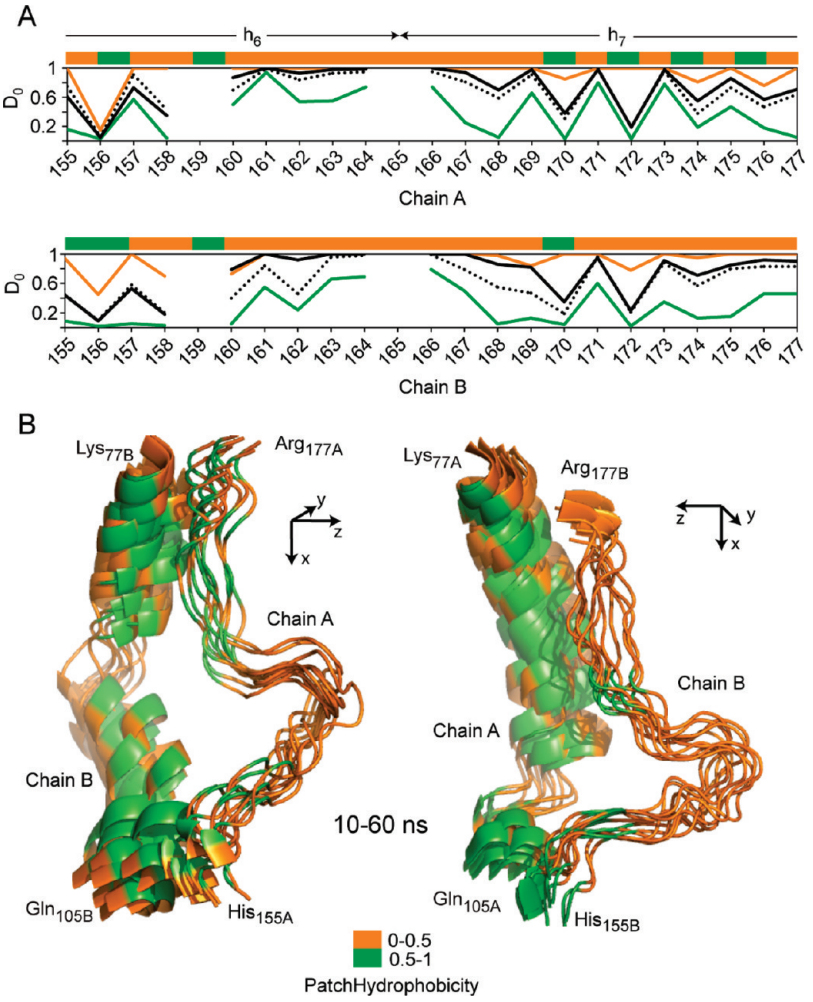

FIGURE 9: Hydrogen−deuterium exchange incorporation factors (D_0) and patch hydrophobicity in the Solar Flare region of apoA1 (H_{155}−R_{177}) that hosts part of helix h_6 (P_{143}−A_{164}) and part of helix h_7 (P_{165}−G_{186}). (A) The top panel shows patch hydrophobicity (top stripe) and a comparison between experimental (black line) and calculated D_0 values for residues in the His_{155}−Arg_{177} region of apoA1 chain A. The orange and green lines identify the maximum and minimum, respectively, for the range of fluctuations of D_0 values calculated from simulation snapshots. The black dotted line shows the average value of calculated D_0 obtained from all 21 snapshots taken during the 60 ns simulation and used for analysis. The bottom panel shows similar information for the His_{155}−Arg_{177} region of chain B of apoA1. These two plots show that the average values of D_0 obtained from the simulation follow the same pattern as the experimentally derived D_0 values and agree well with the latter. (B) For the sake of clarity, this picture shows the superposition of only 11 snapshots of the His_{155}−Arg_{177} region (chains A and B) taken between 10 and 60 ns. The apoA1 chains are shown in cartoon representation. The residues are colored according to their patch hydrophobicity (orange for solvent accessible residues and green for buried residues). The left panel shows the trajectory of the Solar Flare region of chain A (His_{155A}−Arg_{177A}) and the right panel the trajectory of the Solar Flare region of chain B (His_{155B}−Arg_{177B}).

persist for more than 80% of the simulation (Table 3). Table 3 also lists predicted distances between the charged residues of the salt bridges suggested in the original DSH model. Interestingly, some of the salt bridges identified in the original DSH model are very short-lived in the simulation (e.g., Arg_{27A}−Glu_{223B}, Lys_{59A}−Glu_{198B}, and Glu_{62A}−Lys_{195B}), while other salt bridges not observed in the DSH model are predicted to form during the simulation (e.g., Glu_{85A}−Arg_{177B}, Glu_{125A}−Lys_{133B}, and His_{199A}−Asp_{48B}). Among the 28 interchain salt bridges reported in the DSH model (*13*), 12 are found to persist for more than 50% of the simulation.

DISCUSSION

Prolonged molecular dynamics simulation of the DSH model of rHDL supports the major conclusions reached about the structure of nascent HDL based on a multitude of experimental data (SANS, EM, H/D-MS/MS, NMR, distance constraints from FRET, ESR, and MS/MS cross-linking). Notably, the overall superhelical architecture of the protein directly visualized by SANS with contrast variation is retained during the entire simulation despite the change in the overall dimensions of the particle. This scaffolding dictates the organization of the lipid phase of the particle. Importantly, the proposed micellar lipid organization posited in the DSH model is preserved throughout the simulation, though the particle shape changes from prolate ellipsoid to spheroid. The micellar lipid packing proposed is consistent with new experimental ^{31}P NMR data (chemical shift, line shape, and half-line width) on both plasma-isolated HDL and rHDL preparations. The H−D exchange deuterium incorporation factors and H−D exchange rate constants predicted for apoA1 amide hydrogens from the simulation trajectory are also in excellent agreement with the experimental H/D-MS/MS data. Finally, molecular models produced by simulation accommodate a larger number of distance constraints derived from various biophysical experiments than any other model. Thus, lengthy all-atom molecular dynamics simulation suggests the structure posited for nascent HDL in the DSH model is a thermodynamically stable particle with properties

Table 2: Distance Constraints (MS/MS cross-links, FRET, and ESR) in Nascent HDL and Their Fluctuations during Molecular Dynamics Simulation

			simulation[b]		
geometrical constraint	experimental distance (Å)	DSH model[a] distance (Å)	minimum distance (Å)	average distance (Å)	maximum distance (Å)
$W_{50A}-L_{230B}$	FRET (22.7)[c]	22.8[a]	28.2	36.2	46.1
$W_{50B}-L_{230A}$			22.2	28.1	34.2
$W_{72A}-A_{210B}$	FRET (23.5)[c]	30.2	32.9	38.7	49.2
$W_{72B}-A_{210A}$			42.1	48.4	55.1
$L_{90A}-A_{190B}$	FRET (24.0)[c]	26.2	30.8	34.3	39.8
$L_{90B}-A_{190A}$			43.1	48.3	54.3
$W_{108A}-A_{170B}$	FRET (28.8)[c]	26.6	13.8	20.9	28.4
$W_{108B}-A_{170A}$			20.2	25.3	35.3
$Q_{132A}-Q_{132B}$	FRET (30−35)[c]	17.3[d]	1.9	8.3	16.6
$K_{12A}-K_{182B}$	MS/MS (12)[e,g]	16.1	15.9	21.0	26.5
$K_{12B}-K_{182A}$			50.1	59.6	68.4
$K_{40A}-K_{239B}$	MS/MS (12)[e,f,g]	30.1	35.7	41.8	51.0
$K_{40B}-K_{239A}$			26.3	35.7	52.1
$K_{59A}-K_{208B}$	MS/MS (12)[f]	15.6	14.7	23.5	32.6
$K_{59B}-K_{208A}$			21.9	28.5	39.1
$K_{77A}-K_{195B}$	MS/MS (12)[f]	18.1	13.7	19.8	35.0
$K_{77B}-K_{195A}$			35.0	41.5	49.8
$K_{88A}-K_{118B}$	MS/MS (12)[f]	69.1	27.9	64.3	93.8
$K_{88B}-K_{118A}$[h]			62.3	71.2	78.4
$K_{96A}-K_{118B}$[h]	MS/MS (12)[f]	64.2	37.9	63.2	80.1
$K_{96B}-K_{118A}$			63.7	69.5	74.3
$K_{118A}-K_{140B}$	MS/MS (12)[e,f,g]	10.7	4.5	13.4	19.7
$K_{118B}-K_{140A}$			6.4	16.6	26.3
$K_{133A}-K_{140B}$	MS/MS (7.7)[g]	6.4	7.8	12.9	25.2
$K_{133B}-K_{140A}$			12.0	17.6	24.6
$K_{208A}-K_{208B}$[h]	MS/MS (12)[f]	160.1	59.2	89.5	111.5
$K_{133A}-K_{133B}$[i]	ESR (< 15)[e]	6.2	3.0	6.6	12.7
$L_{134A}-L_{134B}$[i]	ESR (< 15)[e]	10.9	6.0	9.2	21.9
$E_{146A}-E_{146B}$[i]	ESR (17−19)[e]	43.8	41.7	47.2	53.2

[a]From ref *13*. [b]The distances reported from simulation do not include any conformational adjustments, like residue free rotation, Cys mutation/attachment of methane thiosulfonate nitroxide spin-label (MTSSL) for ESR, or attachment of 5-{2-[(2-iodo-1-oxoethyl)amino]ethylamino}-1-naphthalenesulfonic acid (AEDANS) acceptor for FRET experiments; rather, they are distances between the extremities of the residues in that particular snapshot from the simulation. [c]From ref *11*. [d]From Lietal.,2001,JBC. [e]From ref *9*. [f]From ref *62*. [g]From ref *61*. [h]This constraint is not compatible with 5/5 registry. [i]Distances between two residues in the DSH model are from the oxygen atom of MTSSL on one residue and the oxygen atom of MTSSL of the other residue.

congruent with experimental data obtained from multiple biophysical platforms.

One of the prominent features of apoA1 architecture in the DSH model of nascent HDL is its superhelical shape. SANS analyses with contrast variation have allowed direct visualization of the protein shape within rHDL. The open helical shape for the antiparallel apoA1 chains appears to form a scaffold upon which lipids assemble in the lipoprotein particle. It should be noted that while the depicted illustration of apoA1 helical conformation has a specific "handedness", programs used for deconvolution of scattering intensities into low-resolution structures cannot distinguish between mirror images of the helical protein (Figure 2 of the Supporting Information) (*65*). This raises an intriguing possibility that an enzymatic reaction like ABCA1-catalyzed nascent HDL formation may actually produce particles containing only one protein helical handedness. Unfortunately, being able to distinguish between HDL particles containing mirror images of the helical apoA1 is beyond the state of the art in the field at present.

One major question raised by our molecular dynamics simulation is the origin for the change in the overall dimensions of the DSH model during simulation, because this feature contradicts direct experimental data (SANS and EM). Previous molecular dynamics simulations of micellar systems have shown similar artifacts [i.e., preference for spherical micelles when molecular mechanics force fields used to describe the intermolecular interactions among polar headgroups are strong relative to weak dispersion interactions among acyl chains (*56*, *57*)]. The force field used in our simulation has been used in multiple prior HDL simulations and was extensively tested on lipids packed as bilayers (*37*, *38*). On the basis of this study, these molecular mechanics parameters may need subtle further refinements to be able to reproduce the overall time-averaged ellipsoidal shape of nascent HDL.

One structural element that no doubt plays an important role in defining apoA1 architecture in nascent HDL is the location and persistence of salt bridges. It is generally believed (*8*) that interchain salt bridges between the amphipathic apoA1 α-helices provide mechanical strength to the particle through dynamic interactions between the two chains, reducing their flexibility in a fashion similar to that of two strands of DNA reversibly tethered together through hydrogen bonds. The results of the molecular dynamics simulation suggest candidate residues that may play an important role in providing structural support to the particle (Figure 12). They also reaffirm the idea of asymmetry in the local structure of the two half-domains of apoA1, which underscores the dissimilarity in the conformations of the two N_t and C_t domains of apoA1, as shown in Figure 11 (bottom). The predicted ends of the two half-domains are distinct, and the N_α- and C_β-termini are predicted to fold back more tightly than the N_β- and C_α-termini.

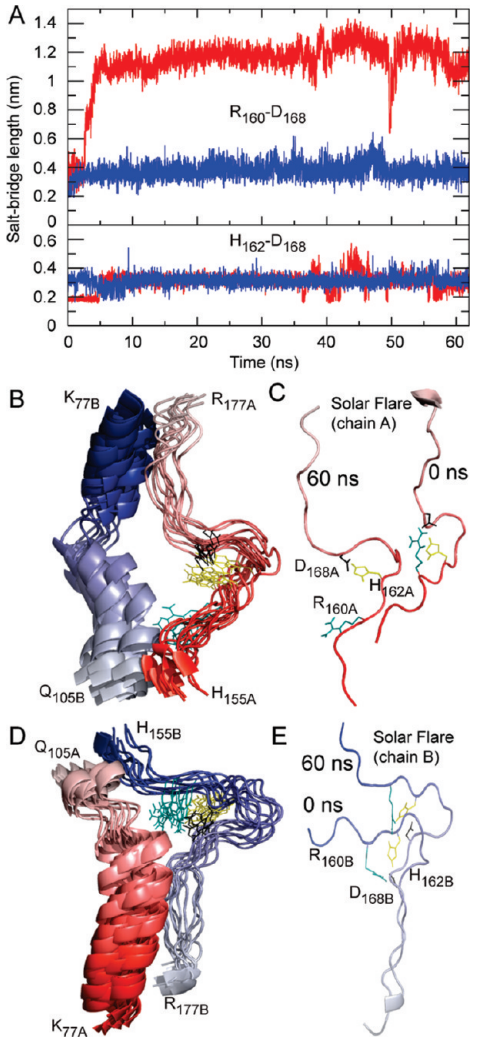

FIGURE 10: Molecular dynamics simulation trajectory of the Solar Flare loops (His_{155}–Arg_{177}) and the predominantly α-helix sequences (Lys_{77}–Gln_{105}), from the adjacent chain of apoA1 in the Double Super Helix model of nascent HDL. The trajectory is composed of 11 snapshots in the 10–60 ns interval. Chain A of apoA1 is colored red and chain B blue, with the color fading from the N- to C-terminus. (A) Fluctuations in the length of R_{160}–D_{168} (top) and H_{162}–D_{168} (bottom, red for chain A and blue for chain B) salt bridges during the simulation. The top graph shows that the R_{160}–D_{168} salt bridge in chain A breaks after approximately 2 ns and remains mainly broken during the entire simulation but is reformed briefly when the simulation reaches 50 ns. On the other hand, the R_{160}–D_{168} salt bridge in chain B is conserved during the simulation. The bottom panel shows that the H_{162}–D_{168} salt bridges in both chains are conserved over the entire simulation. (B) Superposition of the 11 snapshots of the Solar Flare of chain A and the adjacent α-helix of chain B taken during the 10–60 ns period of the simulation. The residues involved in salt bridges are colored and shown as sticks (cyan for R_{160}, yellow for H_{162}, and black for D_{168}). The superposition shows that the Solar Flare conformation (chain A) changes little during the simulation and remains unfolded and solvent exposed as proposed in the Double Super Helix model of HDL. (C) Conformation of the Solar Flare loop (chain A) at the beginning of the simulation (0 ns) and after 60 ns. A comparison of the two snapshots indicates that the shape of the Solar Flare loop remains approximately the same regardless of one salt bridge (R_{160}–D_{168}) being broken. (D) Superposition of the 11 snapshots of the Solar Flare (chain B) and the adjacent α-helix of chain A taken during the 10–60 ns interval of the simulation. This trajectory shows that the two salt bridges are conserved in all frames displayed. (E) Conformation of the Solar Flare loop (chain B) at the beginning of the simulation (0 ns) and after 60 ns. The two snapshots indicate that the shape of the Solar Flare loop remains approximately the same.

Analyses of the simulation trajectory for residues in either intra- or intermolecular salt bridges suggest a large number (more than 80 in each chain) can participate in reversible charge–charge associations within the apoA1 dimer (Figure 12A). Interestingly, 13 residues are observed in each chain of apoA1 to persist for >95% of the simulation within sufficient proximity (4 Å) of a charged counterpart. Of these, four apoA1 residues are predicted to exist within salt bridges throughout the entire simulation in both chains. Remarkably, two of the four are predicted to make a salt bridge within the SF loop and are highly conserved across species [i.e., His_{162}–Asp_{168} (Figure 12B)]. It is also noteworthy that many additional residues that are predicted to form stable salt bridges based upon the simulation are also highly conserved across multiple species (Figure 12B). It is tempting to speculate that these residues may serve essential roles in promoting HDL function, whether it involves generation of a structural element essential for activity of an HDL-associated protein-like LCAT (e.g., as proposed in the case of the His_{162}–Asp_{168} salt bridge within the SF loop) or perhaps by acting as a structural "zipper" that helps to tether the apoA1 chains together. While such salt bridges may provide mechanical strength, their reversible nature also allows for a highly dynamic particle that is capable of adapting and changing shape to meet its function of serving as a carrier of lipid cargo during particle maturation and remodeling.

Another intriguing finding of the molecular dynamics simulation is that while the lipid phase retains micellar packing as in the original DSH model and appears to be thermodynamically stable over the entire simulation, unexpectedly, it develops a noticeable empty cavity at the center of the particle. Frankly, this finding was at first met with skepticism by the authors. However, we were surprised to find that several decades ago, when micellar systems were being intensively structurally studied, that direct experimental data on micelles (*51*–*56*, *66*), including small angle neutron scattering (*67*–*69*) and small angle X-ray scattering (*53*), confirmed the presence of a cavity at the center of some spherical micelles. Moreover, computer simulations (*51*, *54*–*57*) have previously posited the presence of a central void within micelles, and theoretical arguments (*50*) have postulated that it in part arises from the unfavorable packing of acyl chain ends into a small volume at the center of the micelle. Further, simulation models have postulated that the size of this cavity may be minimized in larger micelles by adopting alternative shapes like ellipsoidal and cylindrical micelles (*56*, *57*, *66*).

The shape of the DSH model of nascent HDL is consistent with experimental observation (i.e., SANS and EM). Still, its lipid packing exhibits a small void along the main axis of the ellipsoid. We speculate that the existence of a void at the center of the micellar lipid phase in nascent HDL supports the particle carrier function because the storage of hydrophobic neutral lipids such as cholesterol esters and triglycerides at the center of the particle will require a lower free energy for lipid reorganization. The work required to create a cavity in a condensed system is known in statistical thermodynamics as the free energy of cavity formation (*70*). The central void noted within the micellar structure suggests it may not be necessary to push away as many lipids from the center of the nascent HDL during particle maturation. It is also worth noting that the molecular dynamics simulation studies of the DSH model of nascent HDL are more easily reconciled with one that can be predicted for spherical HDL. It also suggests an overall structure that helps envision how a nascent HDL particle that undergoes maturation starts to accrue

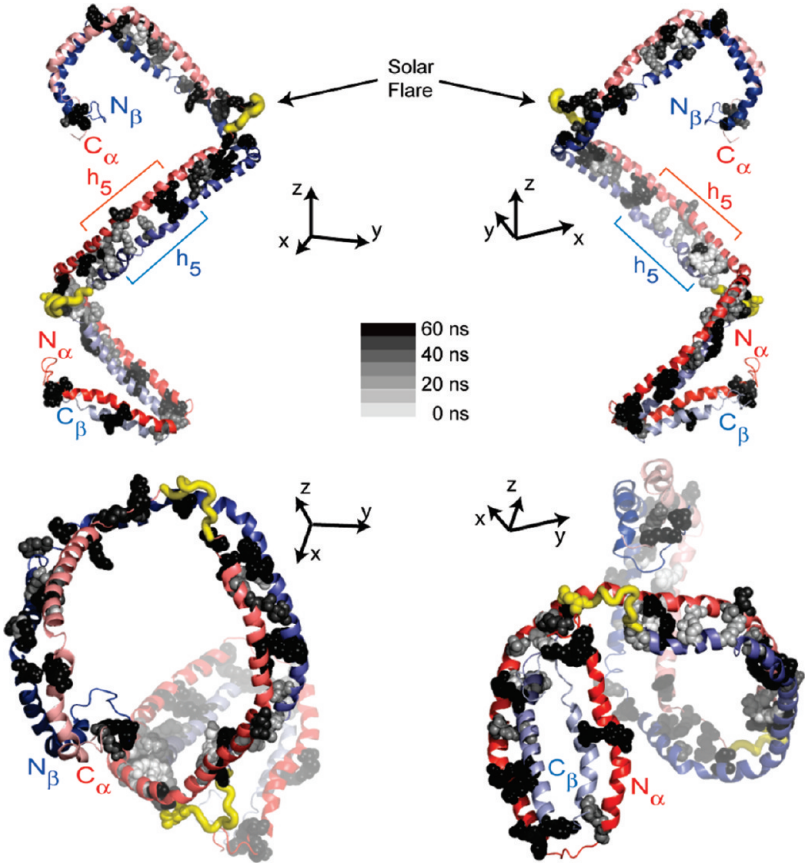

FIGURE 11: Predicted salt bridge distribution in apoA1 during 60 ns of molecular dynamics simulation. The conformation of apoA1 shown from a different vantage point with the N- and C-termini pointing toward and away from the viewer, respectively. The figure shows that the salt bridges located toward the N- and C-termini are more persistent (colored black or dark gray) during simulation while those located in the middle region of apoA1 are less persistent (colored light gray).

neutral lipids in its void core and gradually changes shape from a prolate ellipsoid to a spheroid without altering the overall packing of the lipid phase at the surface, which retains its micellar and pseudolamellar (where protein overlies) organization.

Early seminal studies by Brewer and colleagues more than three decades ago first reported that the ^{31}P NMR spectrum of HDL demonstrates an unusually unique isotropic character compared to that observed in other lipoproteins, indicating that the phospholipids within HDL are far more dynamic than other lipoproteins (*71*). Despite these early studies, further ^{31}P NMR studies into the lipid organization (e.g., lamellar vs micellar) of HDL have not been reported. ^{31}P NMR can be used to distinguish between micellar and lamellar mesophases (*33*, *35*, *58*). This is true because the ^{31}P NMR chemical shift, line shape, and line width arising from the phosphate headgroup of phospholipids in aqueous dispersions are sensitive to the dynamics and organization of model and biological membranes. For example, micellar phase phospholipids show a single sharp isotropic peak at 0 ppm, whereas lamellar, hexagonal array, and multilamellar phases show different chemical shifts and significant line broadening (both upfield and downfield, depending upon the mesophase), consistent with the limitation of rotation of the lipid in these alternative organizations (*33*, *35*, *58*). The sharp isotropic ^{31}P NMR peak at 0 ppm observed in the phospholipid within rHDL and pHDL is consistent with a lipid that is highly dynamic and tumbling in all orientations, more so than what was predicted for a small unilamellar vesicle of a similar size.

From the perspective of biological function, a micellar lipid organization can be more adaptable and flexible than a bilayer. For example, HDL-associated proteins that catalyze direct lipid transfer reactions with the particle will not require any type of mechanism to tackle an asymmetry that becomes inherent in a disk model of HDL (i.e., with two lipid leaflets of a bilayer, there is substantial barrier to "flip-flop", whereas the lipids in a micellar particle can diffuse freely throughout the particle). This limitation in the freedom of motion likely underlies the origins in the differences in isotropic motion of the phospholipid within lamellar (bilayer) phase versus HDL noted in the ^{31}P NMR studies. Finally, a micellar packing of the lipid may actually represent a conserved structural motif among many lipoproteins. For example, Weisgraber and colleagues used SAXS to explore the structure of apolipoprotein E−DPPC particles in solution and observed a spheroidal particle with contorted apolipoprotein E and an ellipsoidal lipid core with phospholipids posited to be packed in a micellar organization (*72*).

Prior models of HDL are characterized by a protein conformation that is highly symmetrical (*6*−*11*). An inference that follows from these models is that HDL-associated proteins can interact on two locations of apoA1 within HDL. In contrast, with the improved resolution afforded by SANS for direct visualization of the protein shape within nascent HDL, the overall conformation of apoA1 in nascent HDL proposed in the DSH model and these simulation studies indicate that the protein helical shape is not symmetric. Interestingly, as experimental data on HDL have accumulated, we see that some regions of apoA1 must have imprinted in them some structural specificity for a high degree of recognition and selectivity for HDL-associated

Table 3: Predicted Interchain Salt Bridges in Nascent HDL during the Molecular Dynamics Simulation

		simulation trajectory			
salt bridge	DSH model distance (Å)	minimum[a] distance (Å)	average[b] distance (Å)	maximum[c] distance (Å)	persistence[d] (%)
$Arg_{10A}-Glu_{234B}$	1.53	2.17	2.72	3.21	14.3
$Lys_{12A}-Glu_{234B}$	1.67	1.97	2.83	3.96	14.3
$Arg_{27A}-Glu_{223B}$	1.68	2.47	2.47	2.47	4.8
$Lys_{40A}-Asp_{213B}$	1.65	2.23	2.50	2.77	57.1
$Asp_{48A}-Lys_{206B}$	1.69	2.19	2.70	3.94	23.8
$Asp_{48A}-Lys_{208B}$	7.25	2.02	3.16	3.85	57.1
$Asp_{51A}-Lys_{206B}$	5.88	3.95	3.95	3.95	4.8
$Lys_{59A}-Glu_{198B}$	1.52	2.30	2.30	2.30	4.8
$Glu_{62A}-Lys_{195B}$	1.61	2.08	2.08	2.08	4.8
$Glu_{70A}-Arg_{188B}$	1.53	1.92	3.07	3.75	57.1
$Lys_{77A}-Glu_{183B}$	1.55	2.03	2.03	2.03	4.8
$Glu_{78A}-Arg_{177B}$	**1.68**	**1.95**	**2.69**	**4.00**	**85.7**
$Glu_{85A}-Arg_{177B}$	10.55	1.95	2.71	3.87	66.7
$Asp_{89A}-Arg_{173B}$	**1.65**	**1.81**	**2.14**	**3.34**	**100**
$Glu_{92A}-Arg_{171B}$	1.53	1.72	2.66	3.99	33.3
$Glu_{92A}-Arg_{173B}$	**1.53**	**1.94**	**2.31**	**3.14**	**95.2**
$Lys_{96A}-Glu_{169B}$	1.56	2.73	2.73	2.73	4.8
$Lys_{107A}-Asp_{157B}$	**1.5**	**2.10**	**2.63**	**3.97**	**80.9**
$Glu_{110A}-Arg_{151B}$	9.11	3.66	3.66	3.66	4.8
$Glu_{111A}-Arg_{151B}$	1.54	2.82	2.82	2.82	4.8
$Glu_{111A}-His_{155B}$	**1.42**	**1.61**	**1.79**	**2.01**	**100**
$Lys_{118A}-Glu_{147B}$	**1.51**	**2.02**	**2.64**	**3.81**	**85.7**
$Glu_{125A}-Lys_{133B}$	10.33	2.03	2.41	3.16	66.7
$Glu_{125A}-Lys_{140B}$	**1.59**	**2.06**	**2.42**	**3.30**	**80.9**
$Glu_{128A}-Lys_{133B}$	10.25	2.26	2.98	3.92	28.6
$Glu_{136A}-Arg_{123B}$	*1.6*	*2.21*	*2.21*	*2.21*	*4.8*
$Lys_{140A}-Glu_{125B}$	*1.76*	*2.23*	*2.50*	*2.77*	*9.5*
$Glu_{147A}-Lys_{118B}$	*1.62*	*2.04*	*2.59*	*3.09*	*33.3*
$Arg_{151A}-Glu_{111B}$	*1.65*	*1.82*	*2.83*	*3.80*	*61.9*
$His_{155A}-Glu_{110B}$	*4.2*	*3.84*	*3.84*	*3.84*	*4.8*
$His_{155A}-Glu_{111B}$	**1.49**	**1.61**	**1.83**	**2.40**	**95.2**
$Asp_{157A}-Lys_{107B}$	*9.2*	*3.90*	*3.90*	*3.90*	*4.8*
$Arg_{171A}-Glu_{85B}$	*7.29*	*3.14*	*3.55*	*3.99*	*19.0*
$Arg_{171A}-Glu_{92B}$	*13.81*	*3.97*	*3.97*	*3.97*	*4.8*
$Arg_{173A}-Glu_{78B}$	*1.51*	*2.27*	*2.58*	*3.45*	*28.6*
$Arg_{173A}-Glu_{85B}$	*5.55*	*2.02*	*2.62*	*3.83*	*38.1*
$Arg_{177A}-Glu_{70B}$	*19.97*	*2.28*	*3.31*	*3.96*	*38.1*
$Arg_{177A}-Asp_{73B}$	*13.68*	*2.95*	*3.47*	*3.95*	*14.3*
$Glu_{191A}-Lys_{59B}$	*1.47*	*2.10*	*2.78*	*3.45*	*66.7*
$Lys_{195A}-Asp_{48B}$	*13.46*	*2.19*	*2.96*	*3.52*	*19.0*
$Lys_{195A}-Asp_{51B}$	*11.74*	*2.10*	*3.26*	*3.96*	*38.1*
$Glu_{198A}-Lys_{45B}$	*8.82*	*3.63*	*3.84*	*3.97*	*14.3*
$His_{199A}-Asp_{48B}$	**6.37**	**1.63**	**1.91**	**2.71**	**95.2**
$Glu_{212A}-Lys_{40B}$	*7.34*	*1.99*	*2.69*	*3.96*	*19.0*
$Asp_{213A}-Lys_{40B}$	*7.64*	*3.08*	*3.08*	*3.08*	*4.8*
$Lys_{238A}-Glu_{2B}$	*2.69*	*2.43*	*3.35*	*3.94*	*42.8*
$Lys_{239A}-Glu_{2B}$	*1.66*	*2.27*	*2.79*	*3.30*	*9.5*

[a]Minimum distance between charged residues detected over the entire trajectory. [b]Average distance between charged residues calculated from all snapshots. [c]Maximum distance between charged residues detected over the entire trajectory. [d]Salt bridge persistence calculated as the fraction of the snapshots in which the salt bridge was detected (i.e., that distance between charged residues was less than 4 Å). Salt bridges in italic rows are located in the half-domain of the apoA1 dimer that contains the N_β/C_α terminal pair. Salt bridges in bold rows persist more than 80% of the simulation.

proteins. For example, myeloperoxidase (MPO), a leukocyte-derived enzyme that binds to HDL in human atherosclerotic plaque and plasma, has been shown to interact with a small region of apoA1 corresponding to residues $Ala_{190}-Leu_{203}$ (*12*). Another example is the site of LCAT interaction on apoA1 of nascent HDL, the SF region (approximately residues $His_{155}-Arg_{177}$) (*12*). While the SF loops are highly dynamic, these regions are predicted by molecular dynamics simulation to be thermodynamically stable when exposed to solvent, and the overall "random coil" loop conformation is conserved during simulation (Figure 10). It is thus remarkable that the two SF loops are predicted to possess distinct structural environments. While there is clearly a high degree of specificity in both MPO and LCAT binding to apoA1 observed experimentally by H/D-MS/MS and peptide competition studies (*12*, *73*), the precise stoichiometries of these and other HDL−HDL-associated protein interactions have not been quantitatively investigated. Our simulation studies show intriguing differences in the two SF regions, suggesting distinct steric environments exist for each loop. This raises the possibility that LCAT may interact preferentially with one of the SFs. Experiments that aim to actually discriminate whether LCAT, MPO, or other HDL-associated proteins differentially bind nascent HDL at more than one site per particle with different affinities are intriguing future

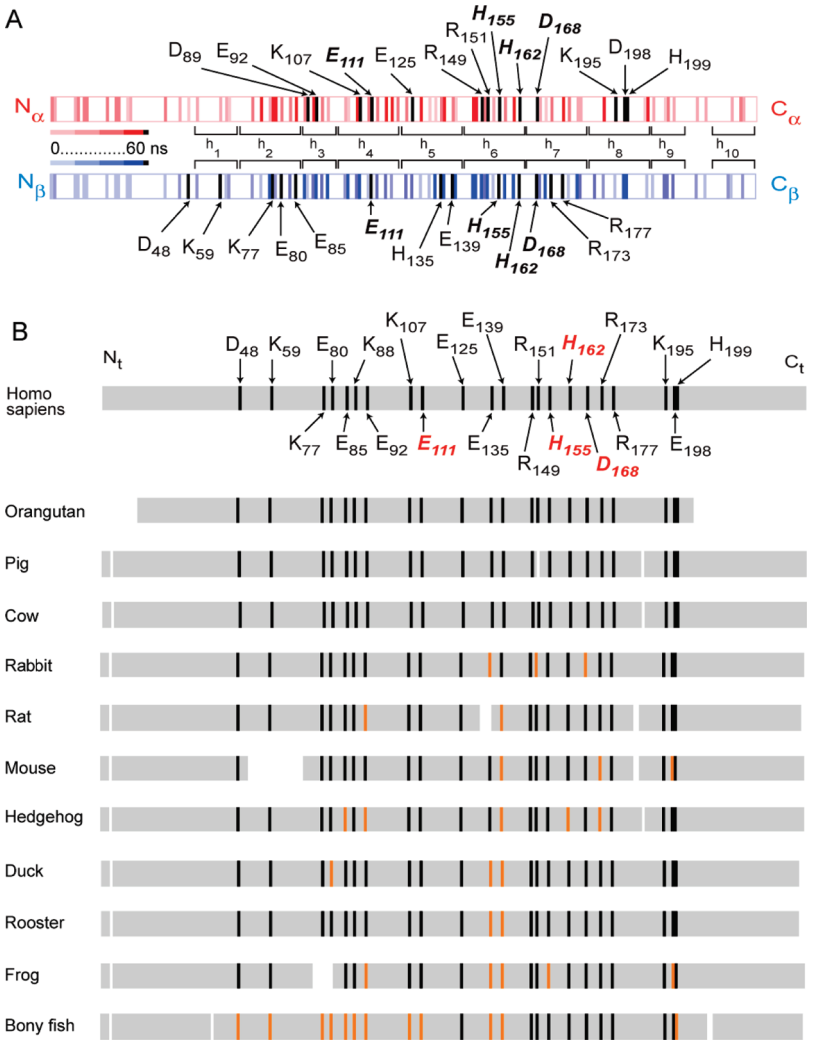

FIGURE 12: Map of charged amino acid residues involved in salt bridges during the simulation and their conservation between species. (A) Distribution of residues predicted to form inter- and intrachain salt bridges in apoA1 during simulation. The apoA1 dimer is shown as a double stripe colored red for chain A and blue for chain B. Residues predicted to be involved in a salt bridge during the simulation trajectory are shown as vertical stripes. The predicted persistence of residues within a salt bridge during the simulation trajectory is indicated by the intensity of the color, lighter color indicating less persistence and darker color greater persistence. Residues that persist more than 95% of the simulation are colored black. (B) Analysis of species conservation of apoA1 residues predicted to persist (> 95%) within inter- and intrachain salt bridges throughout the simulation trajectory. Residues (n = 22) that persist more than 95% of the simulation are indicated on *Homo sapiens* (black), and those that are common to both chains of apoA1 are labeled in red. Multiple-sequence alignment was performed using the COBALT multiple-alignment tool (http://blast.ncbi.nim.nih.gov) of BLASTP (*76*) relative to *H. sapiens*. Of the 22 residues, those showing either identity or conservation within the acid/base side chain group are indicated by a black stripe, whereas those not conserved are shown as an orange stripe. The following additional species were aligned: *Pongo pygmaeus* (orangutan), *Sus scrofa* (pig), *Bos taurus* (cow), *Oryctolagus cuniculus* (rabbit), *Rattus norvegicus* (rat), *Mus musculus* (mouse), *Erinaceus europaeus* (hedgehog), *Anas platyrhynchos* (duck), *Gallus gallus* (rooster), *Xenopus* (frog), and *Anguilla japonica* (bony fish).

possibilities. It is tempting to speculate that the SF loop may serve as a generalized structural motif that facilitates lipid exchange with more than one HDL-associated protein. It remains to be seen if LCAT interacts with just one of the SF loops, and an alternative lipid exchange protein docks at the other SF loop. Further studies are necessary to investigate these hypotheses.

Limitations of the study are worth noting. While tremendous increases in computational power have permitted computer simulation techniques to evolve significantly over the past several decades and their use in structural and computational biology has become more ubiquitous, it is important to keep in mind that simulation techniques, while increasingly sophisticated, have significant limitations. They can test if a proposed molecular model is thermodynamically plausible. However, they cannot easily discriminate among alternative structural models if there are relatively stable alternatives. Molecular dynamics simulations have been performed on alternative structural models of nascent HDL and suggested they are feasible, including the Picket Fence model (*6*) and Multiple-Double Belt Structural models (*8*, *14*, *15*, *17*−*20*, *22*, *64*). Thus, molecular dynamics simulations alone cannot determine what the "true" structure(s) of HDL is. Rather, direct experimental data allow the determination of the overall architecture of the particle. In this regard, none of the alternative models examined by molecular dynamics simulations show structures that match the results of the broad array of biophysical platforms examined in this investigation. The recent application of contrast variation SANS (ref *13* and this work) enables direct visualization of the overall structure of apoA1 within nascent HDL and reveals that the overall architecture of the protein is open and helical. Similarly, the use of ^{31}P NMR in the study of HDL in this investigation reveals that the dynamic motion of the phospholipids within HDL is incompatible with

lamellar phase organization in a particle the size of HDL and indeed is consistent with a micellar organization. It is also worth noting that while the 80 ns simulation performed in this study is the longest yet reported for an all-atom simulation of HDL, it is still short in duration to account for the full dynamics of the particle. Further, on the basis of reported diffusion coefficients for a phospholipid within a small unilamellar vesicle or lipoprotein (*74*, *75*), one can predict that the average diffusion path length of a lipid over 80 ns for a particle the size of HDL is approximately the particle dimension (~100 Å). Thus, one may argue that the system is not fully equilibrated after simulation for 80 ns, in the sense that not all individual phospholipids had a chance to explore the entire volume of the particle on this time scale. We note, however, that the total energy and, most importantly, the rmsd reach a steady state after simulation for 10−20 ns, suggesting that the system reached thermodynamic equilibrium. To produce longer simulations for such large macromolecular assemblies practically requires use of coarse-grained force fields that describe molecules as a collection of beads (and make prior assumptions about secondary structure). While allowing for longer simulations, the simplifications in the force fields required produce additional artifacts. Perhaps the major strength of molecular dynamics simulations is the fact that they can serve as hypothesis-generating exercises and provide insights into what interactions (e.g., salt bridges, hydrogen bonds, hydrophobic contacts, etc.) may account for specific and global structural features.

Structural studies using traditional high-resolution approaches with large macromolecular complexes remain a challenge. The recent introduction of SANS with contrast variation to the HDL field provides much greater resolution for molecular shape than prior data used for modeling, such as crude estimates of particle size derived from native gels, light scattering, electron microscopy, and gel exclusion chromatography. This study also explored the congruency of experimental data from multiple additional and synergistic biophysical methods (e.g., constraints from H/D-MS/MS, mass spectrometry cross-linking, FRET, and ESR) with molecular dynamics simulations. Remarkably, a high degree of concordance was observed between experimental data from all platforms and those predicted by the simulation trajectory. Finally, these studies generate hypotheses in as much that they have identified candidate residues that might play important structural and functional roles and are also notable for being remarkably conserved throughout evolution.

ACKNOWLEDGMENT

Computational resources were provided by the Ohio Supercomputer Center and the National Center for Supercomputer Applications (NCSA, University of Illinois, Urbana, IL).

SUPPORTING INFORMATION AVAILABLE

Small angle neutron scattering intensities [$I(\mathbf{q})$] versus the scattering vector ($\mathbf{q}$) and distance distribution functions [$p(r)$] versus the distance between scattering centers (r) and low-resolution structures of nascent rHDL in 12 and 42% D_2O (Figures 1 and 2) and experimental and calculated per residue deuterium incorporation factors, H−D exchange rate constants, and residue unfolding constants (Table 1). This material is available free of charge via the Internet at http://pubs.acs.org. The following information is also available for download from http://www.lerner.ccf.org/cellbio/hazen/data/- neutron scattering intensities for HDL samples analyzed in 12% and 42% D_2O (text files), low resolution structures of nascent HDL (pdb files), and calculated H/D exchange deuterium incorporation factors for all residues in apoA1 dimer (Excel file).

REFERENCES

1. Tall, A. R., Yvan-Charvet, L., Terasaka, N., Pagler, T., and Wang, N. (2008) HDL, ABC Transporters, and Cholesterol Efflux: Implications for the Treatment of Atherosclerosis. *Cell Metab. 7*, 365–375.
2. Trigatti, B., Rigotti, A., and Krieger, M. (2000) The role of the high-density lipoprotein receptor SR-BI in cholesterol metabolism. *Curr. Opin. Lipidol. 11*, 123–131.
3. Assmann, G., and Gotto, A. M., Jr. (2004) HDL Cholesterol and Protective Factors in Atherosclerosis. *Circulation 109*, III8–III14.
4. Barter, P. J., and Rye, K. A. (2006) Relationship between the concentration and antiatherogenic activity of high-density lipoproteins. *Curr. Opin. Lipidol. 17*, 399–403.
5. Rader, D. J. (2007) Mechanisms of Disease: HDL metabolism as a target for novel therapies. *Nat. Clin. Pract. Cardiovasc. Med. 4*, 102–109.
6. Phillips, J. C., Wriggers, W., Li, Z., Jonas, A., and Schulten, K. (1997) Predicting the structure of apolipoprotein A-I in reconstituted high-density lipoprotein disks. *Biophys. J. 73*, 2337–2346.
7. Koppaka, V., Silvestro, L., Engler, J. A., Brouillette, C. G., and Axelsen, P. H. (1999) The Structure of Human Lipoprotein A-I: Evidence for the "Belt" Model. *J. Biol. Chem. 274*, 14541–14544.
8. Segrest, J. P., Jones, M. K., Klon, A. E., Sheldahl, C. J., Hellinger, M., De Loof, H., and Harvey, S. C. (1999) A detailed molecular belt model for apolipoprotein A-I in discoidal high density lipoprotein. *J. Biol. Chem. 274*, 31755–31758.
9. Bhat, S., Sorci-Thomas, M. G., Alexander, E. T., Samuel, M. P., and Thomas, M. J. (2005) Intermolecular Contact between Globular N-terminal Fold and C terminal Domain of ApoA-I Stabilizes Its Lipid-bound Conformation. *J. Biol. Chem. 280*, 33015–33025.
10. Maiorano, J. N., Jandacek, R. J., Horace, E. M., and Davidson, W. S. (2004) Identification and structural ramifications of a hinge domain in apolipoprotein A-I discoidal high-density lipoproteins of different size. *Biochemistry 43*, 11717–11726.
11. Martin, D. D., Budamagunta, M. S., Ryan, R. O., Voss, J. C., and Oda, M. N. (2006) Apolipoprotein A-I Assumes a "Looped Belt" Conformation on Reconstituted High Density Lipoprotein. *J. Biol. Chem. 281*, 20418–20426.
12. Wu, Z., Wagner, M. A., Zheng, L., Parks, J. S., Shy, J. M., III, Smith, J. D., Gogonea, V., and Hazen, S. L. (2007) The refined structure of nascent HDL reveals a key functional domain for particle maturation and dysfunction. *Nat. Struct. Mol. Biol. 14*, 861–868.
13. Wu, Z., Gogonea, V., Lee, X., Wagner, M. A., Li, X.-M., Huang, Y., Arundhati, U., May, R. P., Haertlein, M., Moulin, M., Gutsche, I., Zaccai, G., DiDonato, J., and Hazen, S. L. (2009) The double super helix model of high density lipoprotein. *J. Biol. Chem. 284*, 36605–36619.
14. Catte, A., Patterson, J. C., Bashtovyy, D., Jones, M. K., Gu, F., Li, L., Rampioni, A., Sengupta, D., Vuorela, T., Niemela, P., Karttunen, M., Marrink, S. J., Vattulainen, I., and Segrest, J. P. (2008) Structure of spheroidal HDL particles revealed by combined atomistic and coarse-grained simulations. *Biophys. J. 94*, 2306–2319.
15. Catte, A., Patterson, J. C., Jones, M. K., Jerome, W. G., Bashtovyy, D., Su, Z., Gu, F., Chen, J., Aliste, M. P., Harvey, S. C., Li, L., Weinstein, G., and Segrest, J. P. (2006) Novel Changes in Discoidal High Density Lipoprotein Morphology: A Molecular Dynamics Study. *Biophys. J. 90*, 4345–4360.
16. Jones, M. K., Catte, A., Patterson, J. C., Gu, F., Chen, J., Li, L., and Segrest, J. P. (2009) Thermal stability of apolipoprotein A-I in high-density lipoproteins by molecular dynamics. *Biophys. J. 96*, 354–371.
17. Klon, A. E., Segrest, J. P., and Harvey, S. C. (2002) Molecular dynamics simulations on discoidal HDL particles suggest a mechanism for rotation in the apo A-I belt model. *J. Mol. Biol. 324*, 703–721.
18. Shih, A. Y., Arkhipov, A., Freddolino, P. L., and Schulten, K. (2006) Coarse grained protein-lipid model with application to lipoprotein particles. *J. Phys. Chem. B 110*, 3674–3684.
19. Shih, A. Y., Arkhipov, A., Freddolino, P. L., Sligar, S. G., and Schulten, K. (2007) Assembly of lipids and proteins into lipoprotein particles. *J. Phys. Chem. B 111*, 11095–11104.
20. Shih, A. Y., Denisov, I. G., Phillips, J. C., Sligar, S. G., and Schulten, K. (2005) Molecular dynamics simulations of discoidal bilayers

assembled from truncated human lipoproteins. *Biophys. J. 88*, 548–556.
21. Gu, F., Jones, M. K., Chen, J., Patterson, J. C., Catte, A., Jerome, W. G., Li, L., and Segrest, J. P. (2009) Structures of discoidal high density lipoproteins: A combined computational-experimental approach. *J. Biol. Chem. 285*, 4652–4665.
22. Rocco, A. G., Gianazza, E., Calabresi, L., Sensi, C., Franceschini, G., Sirtori, C. R., and Eberini, I. (2009) Structural features and dynamics properties of human apolipoprotein A-I in a model of synthetic HDL. *J. Mol. Graphics Modell. 28*, 305–312.
23. Cowieson, N. P., Kobe, B., and Martin, J. L. (2008) United we stand: Combining structural methods. *Curr. Opin. Struct. Biol. 18*, 617–622.
24. Gingras, A. R., Bate, N., Goult, B. T., Hazelwood, L., Canestrelli, I., Grossmann, J. G., Liu, H., Putz, N. S., Roberts, G. C., Volkmann, N., Hanein, D., Barsukov, I. L., and Critchley, D. R. (2008) The structure of the C-terminal actin-binding domain of talin. *EMBO J. 27*, 458–469.
25. Radford, S. E., Dobson, C. M., and Evans, P. A. (1992) The folding of hen lysozyme involves partially structured intermediates and multiple pathways. *Nature 358*, 302–307.
26. Fleishman, S. J., Unger, V. M., and Ben-Tal, N. (2006) Transmembrane protein structures without X-rays. *Trends Biochem. Sci. 31*, 106–113.
27. Zannis, V. I., Chroni, A., and Krieger, M. (2006) Role of apoA-I, ABCA1, LCAT, and SR-BI in the biogenesis of HDL. *J. Mol. Med. 84*, 276–294.
28. Matz, C. E., and Jonas, A. (1982) Micellar complexes of human apolipoprotein A-I with phosphatidylcholines and cholesterol prepared from cholate-lipid dispersions. *J. Biol. Chem. 257*, 4535–4540.
29. Peng, D. Q., Wu, Z., Brubaker, G., Zheng, L., Settle, M., Gross, E., Kinter, M., Hazen, S. L., and Smith, J. D. (2005) Tyrosine Modification Is Not Required for Myeloperoxidase-induced Loss of Apolipoprotein A-I Functional Activities. *J. Biol. Chem. 280*, 33775–33784.
30. Baker, P. W., Rye, K. A., Gamble, J. R., Vadas, M. A., and Barter, P. J. (2000) Phospholipid composition of reconstituted high density lipoproteins influences their ability to inhibit endothelial cell adhesion molecule expression. *J. Lipid Res. 41*, 1261–1267.
31. Guinier, A. (1939) *Ann. Phys. 12*, 161–237.
32. Svergun, D. I. (1999) Restoring low resolution structure of biological macromolecules from solution scattering using simulated annealing. *Biophys. J. 76*, 2879–2886.
33. Cullis, P. R., and de Kruijff, B. (1979) Lipid polymorphism and the functional roles of lipids in biological membranes. *Biochim. Biophys. Acta 559*, 399–420.
34. Luzzati, V., Gulik-Krzywicki, T., and Tardieu, A. (1968) Polymorphism of Lecithins. *Nature 218*, 1031–1034.
35. Li, X. M., Salomon, R. G., Qin, J., and Hazen, S. L. (2007) Conformation of an Endogenous Ligand in a Membrane Bilayer for the Macrophage Scavenger Receptor CD36. *Biochemistry 46*, 5009–5017.
36. Lindahl, E., Hess, B., and van der Spoel, D. (2001) Gromacs 3.0: A package for molecular simulation and trajectory analysis. *J. Mol. Model. 7*, 306–317.
37. Sapay, N., and Tieleman, D. P. (2008) Computer simulation of lipid-protein interactions. *Curr. Top. Membr. 60*, 111–130.
38. Kandt, C., Ash, W. L., and Tieleman, D. P. (2007) Setting up and running molecular dynamics simulations of membrane proteins. *Methods 41*, 475–488.
39. Höltje, M., Förster, T., Brandt, B., Engels, T., von Rybinski, W., and Höltje, H. D. (2001) Molecular dynamics simulations of stratum corneum lipid models: Fatty acids and cholesterol. *Biochim. Biophys. Acta 1511*, 156–167.
40. Berendsen, H. J. C., Postma, J. P. M., van Gunsteren, W. F., and Hermans, J. (1981) Interaction models for water in relation to protein hydration. In Intermolecular Forces (Pullman, B., Ed.) pp 331−342, D. Reidel Publishing Co., Dordrecht, The Netherlands.
41. Darden, T., York, D., and Pedersen, L. (1993) Particle mesh Ewald: An N-log(N) method for Ewald sums in large systems. *J. Chem. Phys. 98*, 10089–10092.
42. Berendsen, H. J. C., Postma, J. P. M., van Gunsteren, W. F., DiNola, A., and Haak, J. R. (1984) Molecular dynamics with coupling to an external bath. *J. Chem. Phys. 81*, 3684–3690.
43. Hess, B., Bekker, H., Berendsen, H. J. C., and Fraaije, J. G. E. M. (1997) LINCS: A linear constraint solver for molecular simulations. *J. Comput. Chem. 18*, 1463–1472.
44. Miyamoto, S., and Kollman, P. A. (1992) Settle: An analytical version of the shake and rattle algorithms for rigid water models. *J. Comput. Chem. 13*, 952–962.
45. Bai, Y., Milne, J. S., Mayne, L., and Englander, S. W. (1993) Primary structure effects on peptide group hydrogen exchange. *Proteins: Struct., Funct., Genet. 17*, 75–86.
46. Chettya, P. S., Mayneb, L., Lund-Katza, S., Stranzc, D., Englander, S. W., and Phillips, M. C. (2009) Helical structure and stability in human apolipoprotein A-I by hydrogen exchange and mass spectrometry. *Proc. Natl. Acad. Sci. U.S.A. 106*, 19005–19010.
47. Hilser, V. J., and Freire, E. (1996) Structure-based Calculation of the Equilibrium Folding Pathway of Proteins. Correlation with Hydrogen Exchange Protection Factors. *J. Mol. Biol. 262*, 756–772.
48. Black, S. D., and Mould, D. R. (1991) Development of hydrophobicity parameters to analyze proteins which bear post- or cotranslational modifications. *Anal. Biochem. 193*, 72–82.
49. Sanner, M. F., Spehner, J.-C., and Olson, A. J. (1996) Reduced surface: An efficient way to compute molecular surfaces. *Biopolymers 38*, 305–320.
50. Dill, K. A., and Flory, P. J. (1981) Molecular organization in micelles and vesicles. *Proc. Natl. Acad. Sci. U.S.A. 78*, 676–680.
51. Bruce, C. D., Berkowitz, M. L., Perera, L., and Forbes, M. D. E. (2002) Molecular dynamics simulation of sodium dodecyl sulfate micelle in water: Micellar structural characteristics and counterion distribution. *J. Phys. Chem. B 106*, 3788–3793.
52. Itri, R., and Amaral, L. Q. (1991) Distance distribution function of sodium dodecyl sulfate micelles by X-ray scattering. *J. Phys. Chem. 95*, 423–427.
53. Lipfert, J., Columbus, L., Chu, V. B., Lesley, S. A., and Doniach, S. (2007) Size and shape of detergent micelles determined by small-angle X-ray scattering. *J. Phys. Chem. B 111*, 12427–12438.
54. Tieleman, D. P., van der Spoel, D., and Berendsen, H. J. C. (2000) Molecular dynamics simulations of dodecylphosphocholine micelles at three different aggregate sizes: Micellar structure and chain relaxation. *J. Phys. Chem. B 104*, 6380–6388.
55. Wendoloski, J. J., Kimatian, S. J., Schutt, C. E., and Salemme, F. R. (1989) Molecular dynamics simulation of a phospholipid micelle. *Science 243*, 636–638.
56. Yoshii, N., and Okazaki, S. (2007) A molecular dynamics study of structure and dynamics of surfactant molecules in SDS spherical micelle. *Condens. Matter Phys. 10*, 573–578.
57. Fujiwara, S., Itoh, T., Hashimoto, M., and Tamura, Y. (2007) Molecular dynamics simulation of micelle formation in amphiphilic solution. *Mol. Simul. 33*, 115–119.
58. Tilcock, C. P., and Cullis, P. R. (1987) Lipid Polymorphism. *Ann. N. Y. Acad. Sci. 492*, 88–102.
59. Traikia, M., Warschawski, D. E., Recouvreur, M., Cartaud, J., and Devaux, P. F. (2000) Formation of unilamellar vesicles by repetitive freeze-thaw cycles: Characterization by electron microscopy and ^{31}P-nuclear magnetic resonace. *Eur. Biophys. J. 29*, 184–195.
60. Englander, S. W. (2006) Hydrogen exchange and mass spectrometry: A historical perspective. *J. Am. Mass Spectrom. 17*, 1481–1489.
61. Bhat, S., Sorci-Thomas, M. G., Tuladhar, R., Samuel, M. P., and Thomas, M. J. (2007) Conformational adaption of apolipoprotein A-I to discretely sized phospholipid complexes. *Biochemistry 46*, 7811–7821.
62. Silva, R. A. G. D., Hillard, G. M., Li, L., Segrest, J. P., and Davidson, W. S. (2005) A mass spectrometric determination of the conformation of dimeric apolipoprotein A-I in discoidal high density lipoproteins. *Biochemistry 44*, 8600–8607.
63. Li, H.-H., Lyles, D. S., Pan, W., Alexander, E., Thomas, M. J., and Sorci-Thomas, M. G. (2002) ApoA-I structure on discs and spheres. Variable helix registry and conformational states. *J. Biol. Chem. 277*, 39093–39101.
64. Shih, A. Y., Sligar, S. G., and Schulten, K. (2008) Molecular Models Need to be Tested: The Case of a Solar Flares Discoidal HDL Model. *Biophys. J. 94*, L87–L89.
65. Svergun, D. I., and Koch, M. H. J. (2003) Small-angle scattering studies of biological macromolecules in solution. *Rep. Prog. Phys. 66*, 1735–1782.
66. Chevalier, Y., and Zemb, T. (1990) The structure of micelles and microemulsions. *Rep. Prog. Phys. 53*, 279–371.
67. Dill, K. A., Koppel, D. E., Cantor, R. S., Dill, J. D., Bendedouch, D., and Chen, S.-H. (1984) Molecular conformations in surfactant micelles. *Nature 309*, 42–45.
68. Cabane, B., and Zemb, T. (1985) Water in the hydrocarbon core of micelles. *Nature 314*, 385–386.
69. Goyal, P. S., and Aswal, V. K. (2001) Micellar structure and intermicelle interactions in micellar solutions: Results of small angle neutron scattering studies. *Curr. Sci. 80*, 972–979.
70. Hill, T. L. (1956) Statistical Mechanics. Principles and Selected Applications, McGraw-Hill, New York.

71. Assmann, G., Highet, R. J., Sokoloski, E. A., and Brewer, H. B., Jr. (1974) ^{13}C Nuclear Magnetic Resonance Spectroscopy of Native and Recombined Lipoproteins. *Proc. Natl. Acad. Sci. U.S.A. 71*, 3701–3705.
72. Peters-Libeu, C. A., Newhouse, Y., Hall, S. C., Witkowska, H. E., and Weisgraber, K. H. (2007) Apolipoprotein E·dipalmitoylphosphatidylcholine particles are ellipsoidal in solution. *J. Lipid Res. 48*, 1035–1044.
73. Zheng, L., Settle, M., Brubaker, G., Schmitt, D., Hazen, S. L., Smith, J. D., and Kinter, M. (2005) Localization of nitration and chlorination sites on apolipoprotein A-I catalyzed by myeloperoxidase in human atheroma and associated oxidative impairment in ABCA1-dependent cholesterol efflux from macrophages. *J. Biol. Chem. 280*, 38–47.
74. Ellena, J. F., Lepore, L. S., and Cafiso, D. S. (1993) Estimating lipid lateral diffusion in phospholipid vesicles from ^{13}C spin-spin relaxation. *J. Phys. Chem. 97*, 2952–2957.
75. Vauhkonen, M., Sassaroli, M., Somerharju, P., and Eisinger, J. (1989) Lateral diffusion of phospholipids in the lipid surface of human low-density lipoprotein measured with a pyrenyl phospholipid probe. *Eur. J. Biochem. 186*, 465–471.
76. Altschul, S. F., Madden, T. L., Schaefer, A. A., Zhang, J., Zhang, Z., Miller, W., and Lipman, D. J. (1997) Gapped BLAST and PSI-BLAST: A generation of protein database search programs. *Nucleic Acids Res. 25*, 5101–5109.